

Ocean Scale Interactions from Space

Patrice Klein^{1,2,3}, Guillaume Lapeyre⁴, Lia Siegelman^{1,2,5}, Bo Qiu⁶, Lee-Lueng Fu¹, Hector Torres¹, Zhan Su², Dimitris Menemenlis¹, Sylvie Le Gentil³

¹Jet Propulsion Laboratory (NASA), California Institute of Technology, Pasadena, USA

²California Institute of Technology, Pasadena, USA

³Lops-Ifremer/CNRS FRANCE

⁴LMD/IPSL,CNES,ENS,PSLRU Paris, FRANCE

⁵LEMAR/IUEM/CNRS, FRANCE

⁶University of Hawaii, USA

Key Points:

- 25 years of satellite altimeter observations and recent numerical studies highlight that all the oceans are fully turbulent.
- This turbulence involves energetic Ocean Scale Interactions over a broad range of scales, from 1km to 5000 km.
- These interactions control the ocean kinetic energy budget, heat storage, biodiversity and air-sea exchanges.

© 2019. All rights reserved.

Corresponding author: Patrice Klein, pklein@caltech.edu or jean.patrice.m.klein-130513@jpl.nasa.gov or patrice.klein@ifremer.fr

18 **Abstract**

19 Satellite observations of the last two decades have led to a major breakthrough emphasizing
 20 the existence of a strongly energetic mesoscale turbulent eddy field in all the oceans.
 21 This ocean mesoscale turbulence (OMT) is characterized by cyclonic and anticyclonic
 22 eddies (with a 100–300 km size and depth scales of ~500–1000 m) that capture approx-
 23 imately 80% of the total kinetic energy and is now known to significantly impact the
 24 large-scale ocean circulation, the ocean’s carbon storage, the air-sea interactions and there-
 25 fore the Earth climate as a whole. However, OMT revealed by satellite observations has
 26 properties that differ from those related to classical geostrophic turbulence theories. In
 27 the last decade, a large number of theoretical and numerical studies has pointed to sub-
 28 mesoscale surface fronts (1–50 km, not resolved by satellite altimeters and not fully taken
 29 into account by geostrophic turbulence theories) as the key suspect explaining these dis-
 30 crepancies. Submesoscale surface fronts have been shown to impact mesoscale eddies
 31 and the large-scale ocean circulation in counter-intuitive ways, leading in particular to up-
 32 gradient fluxes. The ocean engine is now known to involve energetic scale interactions,
 33 over a much broader range of scales than expected one decade ago, from 1 km to 5000
 34 km. New space observations with higher spatial resolution are however needed to validate
 35 and improve these recent theoretical and numerical results.

36 **1 Introduction**

37 In 1992, a satellite with a high-precision altimeter, Topex/Poseidon (T/P, CNES/NASA),
 38 was launched in space to observe the Sea Surface Height (SSH) in all oceans over a range
 39 of scales from 100 km to more than 5000 km. SSH observations, a proxy of surface pres-
 40 sure, were used to retrieve oceanic surface motions using the geostrophic approxima-
 41 tion (that assumes an equilibrium between Coriolis and pressure gradients forces). First
 42 analyses of T/P observations profoundly revolutionized the field of oceanography. They
 43 showed that General Ocean Circulation Models (OGCM) with low spatial resolution were
 44 strongly deficient in estimating the kinetic energy of oceanic motions [*Fu and Smith,*
 45 *1996; Stammer et al., 1996*]. Walter Munk, testifying before the U.S. Commission on
 46 Ocean Policy in April 2002, emphasized that T/P was "the most successful ocean exper-
 47 iment of all time". In September 2018, over three hundred ocean scientists attended a five-
 48 day symposium in Ponta Delgada (Azores Archipelago) to celebrate 25 Years of Progress
 49 in satellite radar altimetry. Ocean monitoring over more than two decades, using T/P and
 50 other satellite altimeters (Figure 1), has led to a major scientific breakthrough responsible
 51 of a paradigm shift: all the oceans are now known to be populated by numerous coherent
 52 eddies at mesoscale (100–300 km) as illustrated by Figure 2a. Altimeter observations fur-
 53 ther emphasize these eddies capture almost 80% of the total oceanic kinetic energy (KE)
 54 of the ocean [*Wunsch, 2002, 2009; Ferrari and Wunsch, 2009; Chelton et al., 2011; Mor-*
 55 *row and Le Traon, 2012*]. Although energetic eddies are present everywhere, they are in-
 56 tensified in hot spots associated with major oceanic currents such as the Gulf Stream, the
 57 Kuroshio Extension and the Antarctic Circumpolar Current (see Figure 2b). This vision of
 58 a strongly turbulent ocean at mesoscale has been confirmed by recent numerical OGCMs
 59 performed with high resolution of a few kilometers (see Figure 3).

61 Due to the high vertical stratification of the open ocean and the Earth rotation, oceanic
 62 motions at scales larger than 100 km are geostrophic and quasi-horizontal [*Vallis, 2017*],
 63 i.e. vertical motions at these scales are very weak. So, it is not surprising that the ocean
 64 mesoscale turbulence (OMT) revealed by satellite altimeters was then expected to obey
 65 the properties of geostrophic turbulence (GT), described in many theoretical and numeri-
 66 cal studies starting with *Charney [1971]* (see e.g. *Rhines [1975], Rhines [1979], Hua and*
 67 *Haidvogel [1986], McWilliams [1989], Hua et al. [1998]*).



60

Figure 1. Existing and future satellite altimeters (see <https://sealevel.jpl.nasa.gov/>).

68

69

70

71

72

73

74

75

76

77

78

79

80

81

82

83

84

85

86

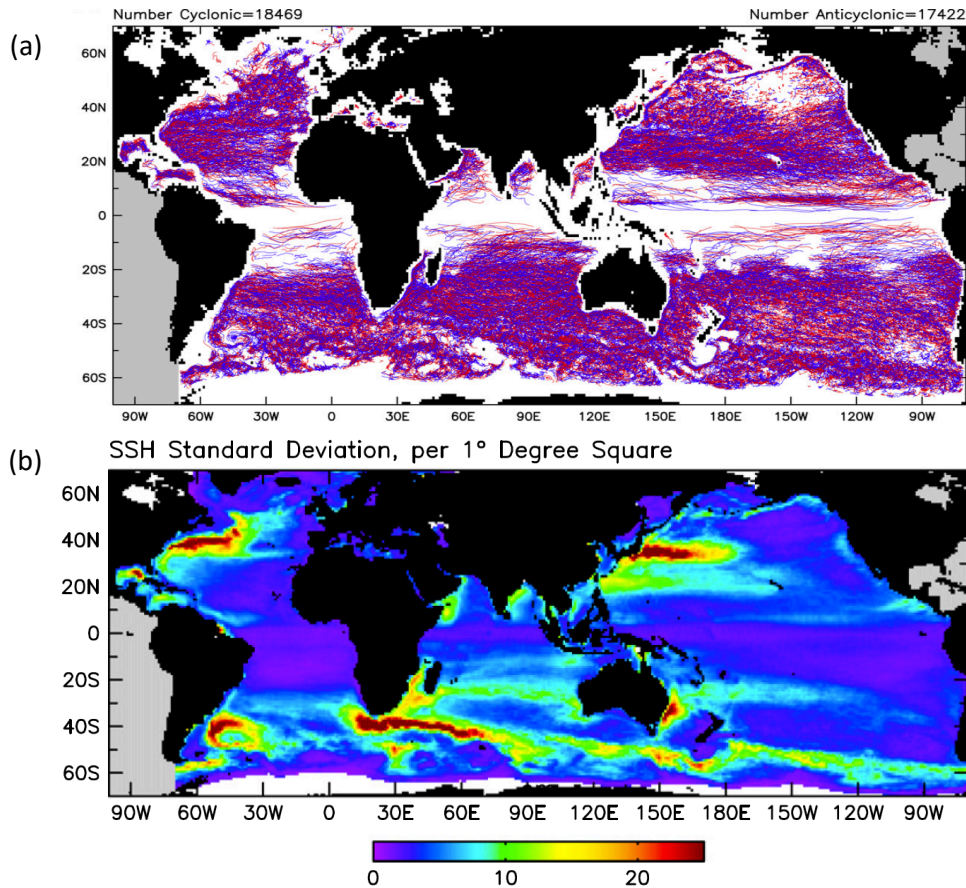
87

88

89

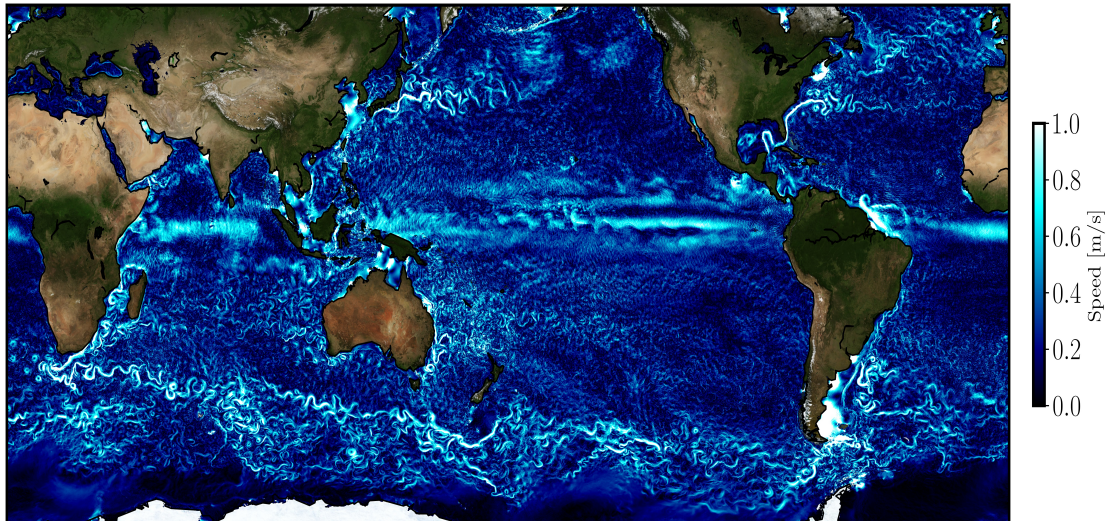
90

Because of the specific impacts of the rotation and vertical stratification, GT properties strongly differ from the classical 3-D turbulence properties [Tennekes and Lumley, 1974]. A first difference is the existence in GT of an inverse KE cascade, driven by the nonlinear interactions between eddies, such that KE fluxes from the scales of eddy sources (mostly explained by baroclinic instability) towards larger scales (for which Rossby wave dispersion starts to dominate and nonlinear interactions weaken). Such inverse KE cascade is concomitant with the nonlinear merging between coherent eddies giving rise to larger ones [Vallis, 2017]. As a consequence, the resulting eddy fluxes significantly increase the total KE and further strengthen large geostrophic eddies by making them more coherent with a longer life time, and ultimately leading to the emergence of zonal jets when Rossby wave dispersion becomes significant [Rhines, 1975; Panetta, 1993]. Such inverse KE cascade is not observed in 3-D turbulence that only experiences a direct KE cascade from KE sources to smaller scales and therefore to dissipation scales [Tennekes and Lumley, 1974]. A second difference is the direct cascade of dynamically passive or active tracers towards small scales driven by geostrophic eddies [Lapeyre et al., 2001]. Through the action of stretching and folding, geostrophic eddies generate long and thin filaments of tracers (as illustrated in the ocean by the chlorophyll or Ertel potential vorticity maps, see Figure 4a,b) that eventually mix with their surrounding environment [Pierrehumbert et al., 1994; Ledwell et al., 1993]. Maps of Finite Size Lyapunov Exponents, or FSLE, are an usual index to materialize these stretching and folding processes (see Figure 4c). The associated mechanisms, called chaotic advection [Aref, 1984; Lapeyre, 2002], make mixing much more efficient than expected from the classical diffusion paradigm used in 3-D turbulence, by at least two to three orders of magnitude [Garrett, 1983].



91 **Figure 2.** a) Trajectories of cyclonic (blue lines) and anticyclonic (red lines) eddies (estimated from altimeter data) over the 16-year period, October 1992 to December 2008, for lifetimes >16 weeks (from *Chelton*
 92 *et al.* [2011]). b) Map of the standard deviation of eddy SSH amplitude (in cm) (from *Chelton et al.* [2011],
 93 used with permission).
 94

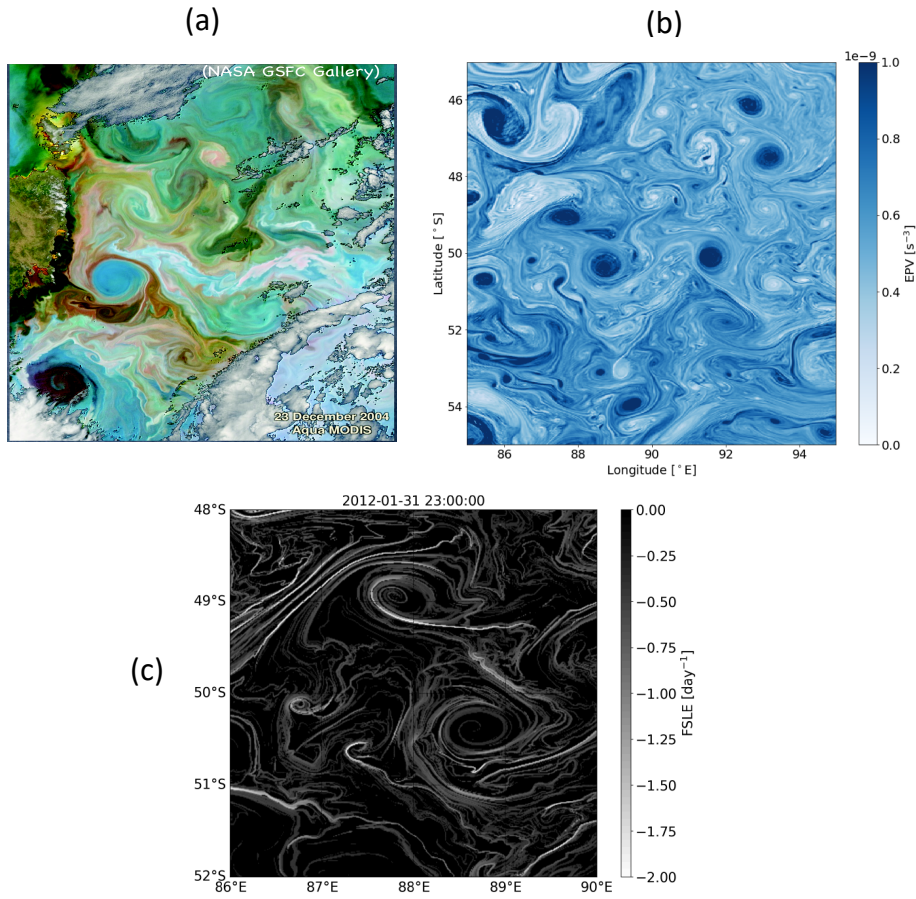
106 Using the GT framework has been illuminating to understand how oceanic mesoscale eddies, observed by satellite, control the global meridional heat transport [*Hausmann and*
 107 *Czaja*, 2012] and how they shape the large-scale ocean circulation through the inverse KE
 108 cascade [*Hurlburt and Hogan*, 2000]. The GT framework has also been used to understand
 109 how OMT drives the three-dimensional dispersion and mixing of tracers, such as
 110 nutrients and therefore the biological diversity and carbon storage [*d'Ovidio et al.*, 2010;
 111 *McGillicuddy Jr*, 2016]. *Mezic et al.* [2010] applied GT ideas to improve the forecast of
 112 pollutants dispersion using altimeter observations. They used these ideas for the forecast
 113 of the oil spill dispersion after the Deep Water Horizon accident in the Gulf of Mexico
 114 (see also *Poje et al.* [2014]). Assimilation of satellite altimeter observations and in-situ
 115 global datasets (such as the ARGO float dataset) in numerical models has led to the fast
 116 development of operational oceanography [*Le Traon*, 2013; *Chassignet et al.*, 2018]. Some
 117 assimilation techniques make use of the GT framework to better represent the OMT
 118 impacts on tracers. For example, *Gaultier et al.* [2012] proposed to assimilate the stretching
 119 (or strain) field (i.e. the second order spatial derivatives of SSH) instead of simply assimilating
 120 SSH. These authors showed how this idea helped to much better predict the chlorophyll
 121 dispersion by mesoscale eddies.
 122



95 **Figure 3.** Instantaneous snapshot of the kinetic energy in the global ocean, from a global ECCO
 96 numerical simulation ($1/48^\circ$ degree resolution in the horizontal and 90 vertical levels). (See
 97 <https://science.jpl.nasa.gov/projects/ECCO-ICES/>).

123 Still, some disconcerting discrepancies between OMT properties diagnosed from SSH ob-
 124 servations and what is expected from GT theory are not fully understood [*Morrow and*
 125 *Le Traon, 2012*] as detailed in section 2. One of the key suspects, highlighted by numer-
 126 ical models with high spatial resolution, is the impact of smaller scales not resolved by
 127 existing satellite altimeters, in particular surface frontal structures with a 1-50 km width
 128 (called submesoscales in the present paper) for which the geostrophic approximation still
 129 works at zero leading order. The numerous numerical and theoretical studies devoted to
 130 submesoscales and their interactions with mesoscale eddies of the past fifteen years, have
 131 led to startling discoveries discussed in section 3. One of them points to the extension of
 132 the inverse KE cascade to scales down to 30 km, i.e. in a regime where frontal processes
 133 are beginning to take place. This suggests the oceans are even less diabatic and more
 134 inertial than we thought, i.e. fluxes are much less controlled by diffusivity or viscosity
 135 (which leads to irreversible down-gradient fluxes) and more by nonlinear interactions that
 136 can lead to reversible up and down gradient fluxes. Mesoscale and submesoscale motions
 137 with scales down to 30 km should be observable by the forthcoming Surface Water and
 138 Ocean Topography (SWOT) altimeter mission [*Fu and Ferrari, 2008*] described in section
 139 4. However, one challenge to meet to analyse these future observations is that balanced
 140 motions with scales smaller than 100 km are entangled with another class of motions, the
 141 internal gravity waves, as discussed in section 5.

142 The most recent results using numerical models with the highest spatial resolution al-
 143 lowed by available peta-scale computers [*Lévy et al., 2010; Chassignet et al., 2017; Su*
 144 *et al., 2018; Torres et al., 2018*] (Figure 3) highlight that ocean scale interactions, involv-
 145 ing scales down to 1 km, affect the ocean dynamics in counter-intuitive ways, as illus-
 146 trated by some examples in section 6. Submesoscale structures in one region not only
 147 impact ocean dynamics locally, but also impact ocean dynamics in remote regions [*Lévy*
 148 *et al., 2010; Chassignet et al., 2017*]. The implication is that understanding how the ocean
 149 engine works, over such a large range of scales, requires a numerical strategy involv-
 150 ing large domains and employing the highest spatial resolution. However, as Carl Wunsch
 151 put it during the OSTST meeting in Lisbon in 2010: "Increased resolution in ocean
 152 models needs to be accompanied by higher resolution observations" on a global scale,



98 **Figure 4.** a) Satellite image of the chlorophyll in the Southern Ocean (see
 99 <https://earthobservatory.nasa.gov/>). (b) Map of the Ertel Potential Vorticity (EPV) in the Southern Ocean
 100 from the global ECCO numerical simulation (see above). EPV is a dynamical active tracer conserved on a
 101 3D Lagrangian trajectory. (c) Map of the Finite Size Lyapunov Exponents (FSLE) in the Southern Ocean
 102 estimated using SSH from the global ECCO numerical simulation ($1/48^\circ$ degree resolution in the horizontal
 103 and 90 vertical levels) (see <https://science.jpl.nasa.gov/projects/ECCO-IcES/>). FSLE are an index of the dis-
 104 persion of tracers and particles by geophysical eddies (with a size of less than 100 km on this map) (see more
 105 details about FSLE in *d'Ovidio et al.* [2010]).

153 which is presently a real challenge, as discussed in section 7. Such observations are in-
 154 deed highly needed to question theories and models in order to improve our understand-
 155 ing of the ocean dynamics, which eventually will lead to new theories and models. The
 156 synergy of using observations from different satellite missions should help to better under-
 157 stand the dynamics involved in this broad range of scales, as discussed in section 7.

158 The purpose of this paper is not to provide a thorough and comprehensive review of the
 159 important contribution of satellite altimeters to the knowledge of the ocean mesoscale tur-
 160 bulance, but rather to point to the missing mechanisms that can potentially improve this
 161 knowledge. The paper mostly focuses on the upper ocean (from the surface down to ~

1000 m) in extra-equatorial latitudes. Equatorial dynamics are discussed in another paper in this issue (see *Menesguen et al.* [2018]).

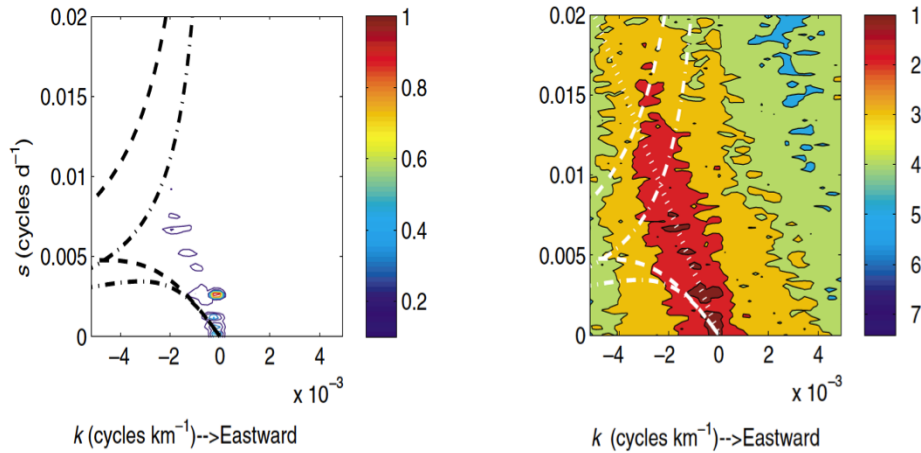
2 Ocean Mesoscale Turbulence and Geostrophic Turbulence Theory

Present altimeter observations concern spatial scales (larger than 70–100 km) for which the associated motions are characterized by a Rossby number (defined as $Ro \equiv U/fL$ with U and L respectively a velocity and length scales and f the Coriolis frequency) smaller than one. This means these surface motions are either in geostrophic balance (i.e. a balance between Coriolis and horizontal pressure forces leading to: $-f\vec{k} \times U = -g\nabla SSH$, with \vec{k} the vertical vector) or in gradient wind balance (a balance that, in addition, involves the nonlinear terms, i.e., $U \cdot \nabla U - f\vec{k} \times U = -g\nabla SSH$) [*Vallis, 2017*].

Balanced motions diagnosed from satellite altimeter observations now concur with the idea that the oceans are fully turbulent, involving strongly interacting mesoscale eddies and giving rise to significant energy transfers across scales. This turbulent character was revealed by one of the first $\omega - k$ spectrum (with ω the frequency and k the horizontal wavenumber) of ocean variability estimated from SSH observations [*Wunsch, 2009, 2010*]. As illustrated by Figure 5, the maximum of the SSH variance does not follow the dispersion relation curves associated with linear Rossby waves. Rather, it lies approximately along a 'non-dispersive' line, $c.k + \omega = 0$ (with $k < 0$), corresponding to an eddy propagation speed of $c \approx 4.6$ cm/s (close to the values found independently by *Fu* [2009]). This finding highlights the strong nonlinear character of mesoscale eddies, confirmed later on by the study of *Chelton et al.* [2011]. All these results point to the existence of an energetic OMT expected to share the GT properties described in *Charney* [1971], *Hua and Haidvogel* [1986], *McWilliams* [1989] and *Hua et al.* [1998]. However, some intriguing discrepancies between OMT and GT properties quickly emerged. Let us comment on two of them.

The first one concerns the KE spectral slope estimated from satellite altimetry. Based on the GT theory, the KE spectrum should scale in k^{-3} [*Charney, 1971*]. However, KE spectra deduced from altimeter observations using the geostrophic balance do display a linear slope in log-log space in the scale range 100 – 300 km, but with a power law varying between k^{-2} and k^{-3} . This discrepancy, early noted by *Fu* [1983], was first attributed to altimeter noise. But, more careful estimations, using a larger set of altimeter observations, by *Le Traon et al.* [2008] confirmed the k^{-2} slope. Such slope for the KE spectrum suggests that smaller eddies resolved by satellite altimeters are more energetic than predicted by GT. *Xu and Fu* [2012] recently highlighted an even more complex picture displaying a strong regional dependency of the SSH spectral slope (Figure 6). On one hand, in many high KE regions, the resulting KE spectral slopes vary between k^{-3} and k^{-2} . On the other hand, in low KE regions, such as in the eastern part of ocean basins, the spectral slope is even flatter than k^{-2} , which is unrealistic in terms of geostrophic motions [*Xu and Fu, 2012*]. The consensus that presently emerges is that this diversity of spectral slopes is not due to altimeter noise, but is due to physical mechanisms other than those involved in GT, that vary seasonally and regionally [*Xu and Fu, 2012; Dufau et al., 2016*].

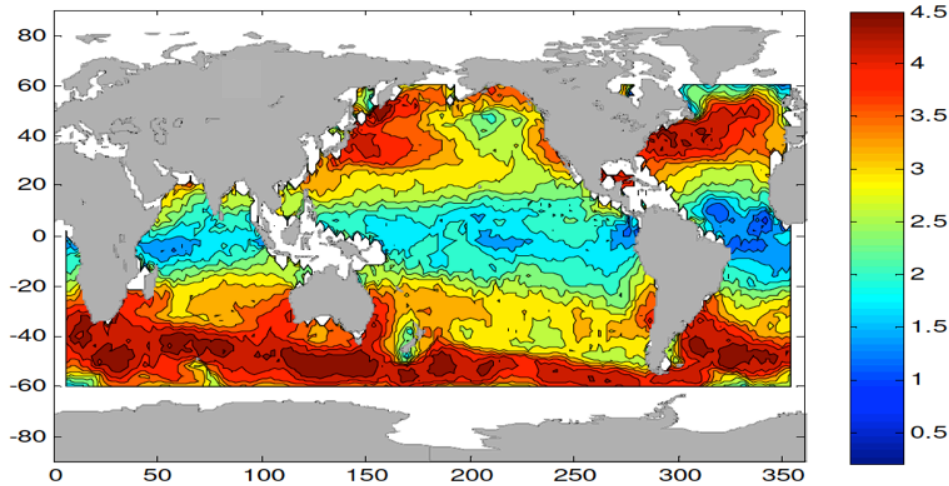
Another discrepancy concerns the KE fluxes or the inverse KE cascade. As mentioned before, GT theory suggests mesoscale geostrophic eddies should experience an inverse KE cascade, with KE fluxing from the scales of eddy sources (50 – 100 km for the ocean) to the scales of the most energetic eddies ($L_e \sim 250$ –300 km for oceanic mesoscale eddies) [*Charney, 1971; Rhines, 1975; Hua and Haidvogel, 1986; McWilliams, 1989; Hua et al., 1998*]. Studies by *Smith* [2007] and *Tulloch et al.* [2011], using altimeter observations and in-situ data, confirmed the factor three to four between the eddy source scales and scales of the most energetic eddies, suggesting an inverse KE cascade over a broad scale range. However, the first KE fluxes estimated from altimeter observations by *Scott and Wang* [2005] were not consistent with this picture. Rather, these authors found an



187 **Figure 5.** Frequency (cycle/day) and zonal wavenumber (cycles/km) spectrum of SSH variance estimated
 188 from altimeter data. The left panel is a two-dimensional spectrum plotted on a linear power scale, smoothed
 189 in frequency and zonal wavenumber. The right panel displays the logarithm of the power. Dashed curves
 190 indicate the barotropic and first baroclinic mode dispersion curves of Rossby waves. Dash-dot lines are the
 191 corresponding curves for the unit aspect ratio. The 'non-dispersive line' defined in the text lies along the
 192 ridge of maximum energy density and is closely approximated by the dotted white line (in the red area of the
 193 right panel) with a slope of 4 km/d (from Wunsch [2009, 2010], © La Societe Canadienne de Meteorologie et
 194 d'Océanographie, reprinted by permission of Taylor & Francis Ltd, www.tandfonline.com on behalf of La
 195 Societe Canadienne de Meteorologie et d'Océanographie.).

225 inverse KE cascade over a narrower scale range, i.e. starting only at wavelengths larger
 226 than 150 km, the smaller wavelengths (including the eddy source scales) experiencing a
 227 direct KE cascade (Figure 7a). Some studies, such as *Arbic et al.* [2012] and *Arbic et al.*
 228 [2013], questioned the contribution of smaller scales, unresolved by altimeter observations,
 229 for the transfer of energy between scales. Using an OGCM with a $1/32^\circ$ spatial resolu-
 230 tion, they showed that the scale range and magnitude of the inverse KE cascade is strongly
 231 sensitive to the resolution of small scales: when small scales are taken into account, the
 232 inverse KE cascade involves a much broader scale range involving smaller scales. Thus,
 233 KE at scales unresolved by satellite altimeters may contribute to KE fluxes that strengthen
 234 eddies resolved by altimetry through the inverse KE cascade. This contribution of unre-
 235 solved scales seems to be in agreement with the $\sim k^{-2}$ spectral slope previously men-
 236 tioned and as further detailed in section 3. Note that, in terms of inverse KE cascade,
 237 *Arbic et al.* [2012] are the first authors to show that OMT experiences an inverse KE cas-
 238 cade in frequency as well.

239 For larger scales, OMT properties appear to match GT properties. One example concerns
 240 the arrest of the inverse KE cascade which leads, from GT, to the emergence of alternat-
 241 ing zonal jets with a width close to the Rhines scale, i.e. the scale at which the Rossby
 242 wave dispersion starts to dominate and the nonlinear interactions weaken [*Rhines*, 1975;
 243 *Hua and Haidvogel*, 1986; *Panetta*, 1993; *Vallis*, 2017]. *Maximenko et al.* [2005, 2008]
 244 tested their existence using satellite altimeter observations averaged over more than ten
 245 years (which filters out mesoscale eddies). Results reveal the presence of multiple zonal
 246 jets, with an east-west velocity direction alternating with latitude, in many parts of the
 247 world oceans [*Maximenko et al.*, 2005, 2008]. At mid-latitudes, jets have often a merid-
 248 ional wavelength close to or larger than 300 km, i.e. close to the Rhines scale.



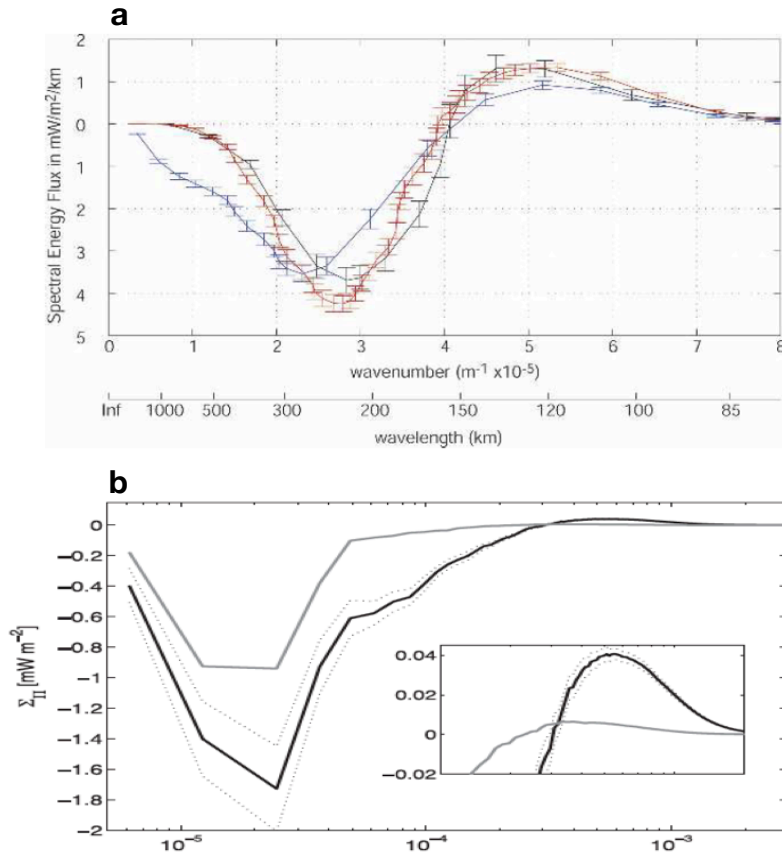
212 **Figure 6.** Global distribution of the spectral slopes (k^{-n}) of SSH wavenumber spectrum in the wavelength
 213 band of 70–250 km estimated from the Jason-1 altimeter measurements. The color scale is related to values of
 214 n (from *Xu and Fu* [2012], © American Meteorological Society. Used with permission).

260 The second example concerns the vertical eddy scale. The combination of SSH and moorings
 261 observations [*Wunsch, 2009, 2010; Wortham and Wunsch, 2014*] shows that roughly
 262 40% of the KE at mesoscale is barotropic in nature, with about another 40% lying in the
 263 first baroclinic mode. Since the buoyancy frequency, $N(z)$, in the ocean is surface in-
 264 tensified, the KE contribution of the first baroclinic mode is also intensified there, lead-
 265 ing to the conclusion that KE inferred from altimeter observations is primarily (but not
 266 wholly) in the first baroclinic mode [*Hua et al., 1985; Wunsch, 2010*]. In other words, KE
 267 at mesoscale concentrates in the first 500–1000 meters below the surface in agreement
 268 with the GT theory and numerical studies of *Fu and Flierl* [1980], *Hua and Haidvogel*
 269 [1986] and *Smith and Vallis* [2001]. As found by these studies, the energy is rapidly trans-
 270 ferred from high to lower baroclinic modes, leading to an inverse KE cascade that is not
 271 only 2D but also 3D in space.

272 As a summary, altimeter observations reveal that OMT shares some similarities with GT,
 273 but also point to some discrepancies. Present studies indicate that many of these discrep-
 274 ancies, in particular in high KE regions, are likely explained by the missing contribution
 275 of unresolved small scales of balanced motions that concern submesoscale density fronts
 276 at the ocean surface as discussed in section 3. On the other hand, discrepancies in low
 277 KE regions seem to be due to the contribution of internal gravity waves, as discussed in
 278 section 5.

279 **3 Ocean Meso/Submesoscale Turbulence: a New Paradigm Involving Submesoscale** 280 **fronts**

281 It has been acknowledged for a long time that the formation and development of atmo-
 282 spheric storms (the equivalent of ocean mesoscale eddies) can only be understood by tak-
 283 ing into account density fronts with smaller scales at the troposphere’s boundaries (i.e. the
 284 Earth surface and the tropopause). The turbulence associated with this boundary frontal
 285 dynamics [*Hoskins, 1976*] was first studied by *Blumen* [1978] who developed a Surface
 286 Quasi-Geostrophic (SQG) theory. SQG theory assumes zero PV in the fluid interior with
 287 the flow being driven by the time evolution of density at the boundaries, leading to intense
 288 fronts at scales smaller than the Rossby radius of deformation [*Held et al., 1995*]. SQG



249 **Figure 7.** a) Spectral kinetic energy flux vs total wavenumber estimated from altimeter data. Black curve
 250 using SSH on a 32x32 grid, red curve using SSH on a 64x64 grid, blue curve using velocity on a 64x64 grid.
 251 Positive slope reveals a source of energy. The larger negative lobe reveals a net inverse cascade to lower
 252 wavenumber. Error bars represent standard error. (From *Scott and Wang* [2005], © American Meteorological
 253 Society. Used with permission). b) Spectral kinetic energy flux (from numerical simulations) integrated over
 254 the upper 200 m for a flow forced by the Charney instability (and therefore involving submesoscale frontal
 255 structures) (solid black) and a flow forced by Phillips instability (and therefore with no submesoscale struc-
 256 ture) (solid gray). Uncertainty is represented as dotted lines based on the assumption that the 360-day run
 257 corresponds to 12 independent realizations. In the inset, the vertical axis is zoomed in the range of large
 258 wavenumbers to better emphasize the forward cascade. (from *Capet et al.* [2016], © American Meteorologi-
 259 cal Society. Used with permission). Similar results are found in *Sasaki et al.* [2014].

289 turbulence was used to explain the dynamics of the atmospheric tropopause by *Juckes*
 290 [1994] and *Hakim et al.* [2002].

291 The impact of surface density fronts at submesoscale on the ocean mesoscale turbulence
 292 started to be questioned only in the early 2000's. Subsequent studies were based on the
 293 theoretical results obtained for the atmosphere and in particular on the SQG theory. Al-
 294 though it has obvious limitations and shortcomings, such as an underprediction of the am-
 295 plitude of subsurface velocities (see *LaCasce* [2012] for example), SQG dynamics coupled
 296 with GT à la Charney [*Tulloch and Smith*, 2006] has been a helpful dynamical frame-
 297 work to understand the interactions between submesoscale dynamics and mesoscale ed-
 298 dies. But later studies have revealed a more complex picture as detailed below.

299

3.1 Surface Frontal Dynamics

300

301

302

303

304

305

306

307

308

309

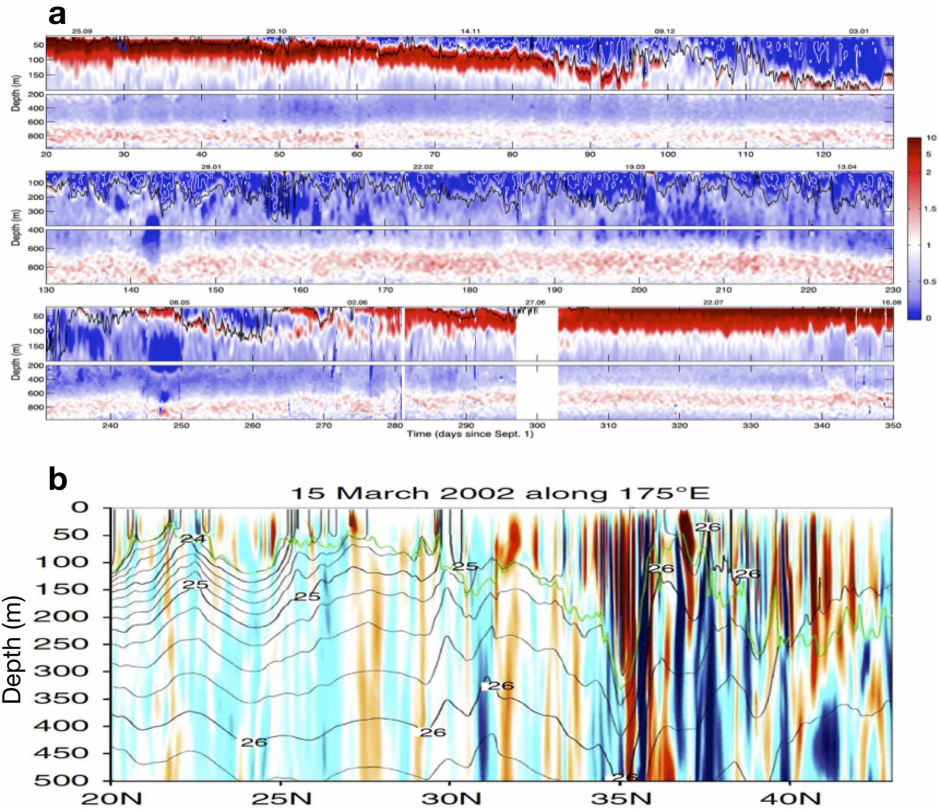
310

311

312

313

Within the oceanic context, early 2000's numerical models [Lévy *et al.*, 2001], that resolved scales down to 10 km, pointed to an appealing property of surface density fronts at submesoscales. These fronts are intimately associated with large vertical velocities extending from surface down to a depth of at least 300–500 m, with values much larger than those reported for 3D geostrophic turbulence, but close to those reported for SQG turbulence [Klein and Lapeyre, 2009]. Two other properties of SQG turbulence, that address the discrepancies mentioned before, led to studies focused on near-surface fronts at submesoscales and their interactions with mesoscale eddies using the SQG paradigm (starting in 2006 with LaCasce and Mahadevan [2006], Lapeyre and Klein [2006] and Lapeyre *et al.* [2006]): the first property is the $k^{-5/3}$ KE spectrum of SQG turbulence [Blumen, 1978; Held *et al.*, 1995], instead of a k^{-3} spectrum for 3D geostrophic turbulence or 2D turbulence. The second property is that an SQG flow experiences an inverse KE cascade [Capet *et al.*, 2008], starting at submesoscale, indicating that submesoscale fronts may energize larger scales.



314

315

316

317

318

319

320

Figure 8. a) Year-long time series of Ertel Potential Vorticity (10^{-9} s^{-3}), calculated from glider data in the Northeastern Atlantic ocean. The time series is divided into (top) fall, (middle) winter and (bottom) spring-summer periods; calendar dates (dd.mm) are provided along the top of the panels. The black contour is the mixed layer depth. (from Thompson *et al.* [2016], © American Meteorological Society. Used with permission). b) Meridional section of vertical velocity in the Northwestern Pacific (from a numerical simulation): vertical velocity (colour, m/day), potential density (black contour) and MLD (green line). (from Sasaki *et al.* [2014]).

321 Later on, a large number of studies quickly revealed that the production of oceanic subme-
 322 sosal scale fronts and their interactions with mesoscale eddies may result from mechanisms
 323 different from SQG. Thus, *Boccaletti et al.* [2007] and *Fox-Kemper et al.* [2008], among
 324 others, revisited previous results from *Stone* [1966] who described baroclinic instabilities
 325 within atmospheric boundary layers. They showed that similar instabilities occur within
 326 the oceanic surface mixed-layer during winter when it is deep. These mixed-layer instabil-
 327 ities (or MLIs) lead to the production of numerous intensified submesoscale fronts during
 328 this period. Seasonality of submesoscale fronts has been confirmed by in-situ observa-
 329 tions in the North Atlantic [*Callies et al.*, 2015; *Thompson et al.*, 2016] (see Figure 8a)
 330 and further detailed by several oceanic numerical models at a basin scale [*Mensa et al.*,
 331 2013; *Sasaki et al.*, 2014; *Qiu et al.*, 2014; *Rocha et al.*, 2016a; *Chassignet et al.*, 2017]
 332 (and also, Julien Le Sommer, personal communication). *Klein et al.* [2008], *Rouillet et al.*
 333 [2012], *Qiu et al.* [2014] and *Capet et al.* [2016] pointed to another mechanism, a cou-
 334 pled surface/interior baroclinic instability (the so-called *Charney* [1947] instability), able
 335 to produce submesoscale fronts near the surface (a mechanism also emphasized by *Tulloch*
 336 *et al.* [2011]). Recently, *Barkan et al.* [2017] further discussed how the high-frequency part
 337 of the wind forcing can also trigger frontal instabilities at submesoscale.

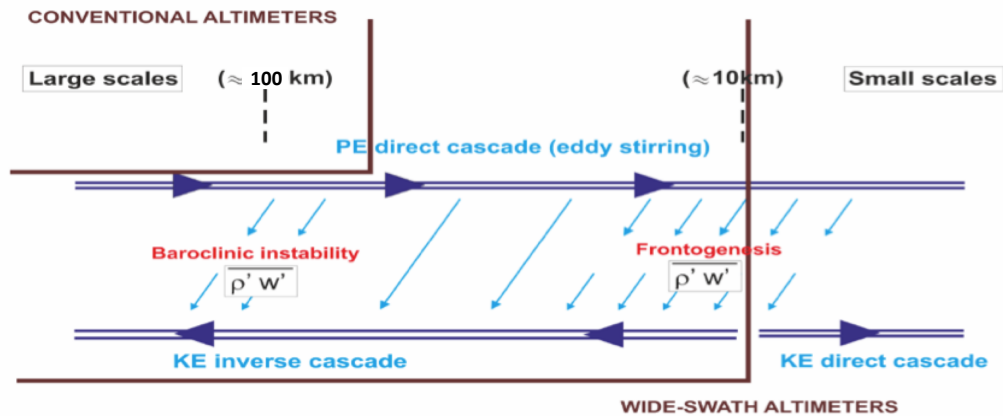
338 In most of these studies, the driving mechanism for the production of submesoscale fronts
 339 is the action of the geostrophic strain on the surface buoyancy gradients which leads to
 340 intensified horizontal fronts and strong vertical motions. It turns out these fronts, whatever
 341 mechanisms that produce them, have properties close to SQG turbulence, such as a tight
 342 relation between buoyancy and relative vorticity (see figure 7 of *Klein et al.* [2008]) and
 343 a $\sim k^{-2}$ (i.e. close to $k^{-5/3}$) KE spectrum slope associated with an inverse KE cascade
 344 starting at submesoscales. Some extensive reviews have been recently dedicated to surface
 345 frontal dynamics at submesoscale in the oceans such as those by *McWilliams* [2016], and
 346 *Lapeyre* [2017].

327 **3.2 Coupling Between Surface Frontal Turbulence and Ocean Mesoscale Turbu-** 328 **lence: a New Energy Route Involving Submesoscales**

329 Whereas mesoscale eddies capture most of the horizontal motions (horizontal KE), sub-
 330 mesoscale fronts are now known to capture most of the vertical velocity field (vertical
 331 KE) in the upper ocean, i.e. in the first 500–1000m below the surface [*Klein et al.*, 2008;
 332 *Thompson et al.*, 2016; *McWilliams*, 2016] (see also Figure 8b). This important prop-
 333 erty, that can be demonstrated using SQG and QG arguments (see Figure 10 in *Klein and*
 334 *Lapeyre* [2009]), has been confirmed by several numerical models at a basin or global
 335 scale [*Sasaki et al.*, 2014; *Su et al.*, 2018] (see Figure 8b). As *Ferrari* [2011] put it: "these
 336 small-scale surface fronts are the equivalents of the thin ducts in the lung called aveoli
 337 that facilitate the rapid exchange of gases when breathing". Near-surface submesoscale
 338 fronts are now thought to be the preferential path of heat, nutrient and other gas exchanges
 339 between the ocean interior and surface. In addition, vertical velocity associated with sub-
 340 mesoscale fronts impacts the energy route. Indeed, vertical fluxes of buoyancy (or density)
 341 driven by submesoscale frontogenesis near the ocean surface correspond to a transforma-
 342 tion of potential energy (PE) into KE that scales as $\overline{w\rho} \propto |\nabla\rho|^2$ with w the vertical ve-
 343 locity and ρ the density (see *Lapeyre et al.* [2006], *Capet et al.* [2008] and *Fox-Kemper*
 344 *et al.* [2008] for this scaling). Since the density spectrum near the surface has a k^{-2} slope
 345 [*Fox-Kemper et al.*, 2008; *Sasaki et al.*, 2014], and therefore $\nabla\rho$ has a flat spectrum, this
 346 means $\overline{w\rho}$ is captured by the smallest scales [*Klein and Lapeyre*, 2009]. In terms of en-
 347 ergy exchanges, the picture that emerges is a tight interaction between oceanic mesoscale
 348 eddies and submesoscale motions that leads to more energetic mesoscales eddies. Indeed,
 349 as sketched in Figure 9 (upper part), mesoscale eddies stir and stretch the surface density
 350 field leading to the production of surface density anomalies at smaller and smaller scales
 351 (a process called direct PE cascade) and therefore to the production of fronts at subme-
 352 soscale. These submesoscale fronts give rise to vertical fluxes of density, and therefore to
 353 a transformation of PE into KE at submesoscale. A large part of this KE at submesoscale

374 is then transferred to mesoscale eddies through the inverse KE cascade [Capet *et al.*, 2016]
 375 (see Figure 7b and lower part of Figure 9).

376 The energy route involving submesoscale density fronts can be coupled with the energy
 377 route à la Salmon [Salmon, 1980], i.e. the one associated with geostrophic turbulence
 378 involving a transformation of PE into KE at the Rossby radius of deformation (i.e. at
 379 mesoscale) through baroclinic instability, as sketched on Figure 9. Such coupling has been
 380 proposed by several studies [Tulloch and Smith, 2006; Callies *et al.*, 2016]. The result-
 381 ing energy route and the associated ocean scale interactions now include a much broader
 382 range of scales (Figure 9) with the inverse KE cascade now starting at submesoscales, as
 383 shown by Capet *et al.* [2016] (Figure 7b). This inverse KE cascade over a broad scale
 384 range reconciles with the findings of Smith [2007] and Tulloch *et al.* [2011] and is also
 385 consistent with the results from Arbic *et al.* [2013] mentioned before. As sketched on Fig-
 386 ure 9, future wide-swath satellite altimeters (such as SWOT, see section 4) should resolve
 387 not only the eddy generation scales but also a large part of submesoscales, and therefore
 388 this inverse KE cascade.



389 **Figure 9.** Schematic of the energy route involving mesoscales and submesoscales. PE is known to experi-
 390 ence a direct cascade from large to small scales because of the eddy stirring (see upper line). The new energy
 391 pathway involving submesoscales includes a transformation of PE into KE at fine-scale (~ 10 – 20 km) due to
 392 frontogenesis and an inverse KE cascade over a wide spectral range (see lower line). Conventional satellite
 393 altimeters only capture the classical energy pathway involving interior baroclinic instability at mesoscale
 394 (down to 100 km). Future wide-swath altimeters, such as SWOT, should capture the energy pathway involving
 395 finer scales (down to ~ 10 – 20 km).

396 The inverse KE cascade over such a broad scale range has been questioned when the
 397 strong ageostrophic character of submesoscale fronts is taken into account (see Molemaker
 398 *et al.* [2010] for a discussion). So far, most numerical models at a basin or a global scale,
 399 using primitive equations with resolution up to 1–3 km [Mensa *et al.*, 2013; Qiu *et al.*,
 400 2014; Sasaki *et al.*, 2014; Rocha *et al.*, 2016b,a; Capet *et al.*, 2016; Su *et al.*, 2018], take
 401 into account this ageostrophic character. They point to a transition scale, between the in-
 402 verse and the direct KE cascade, close to 20–30 km in terms of wavelength depending

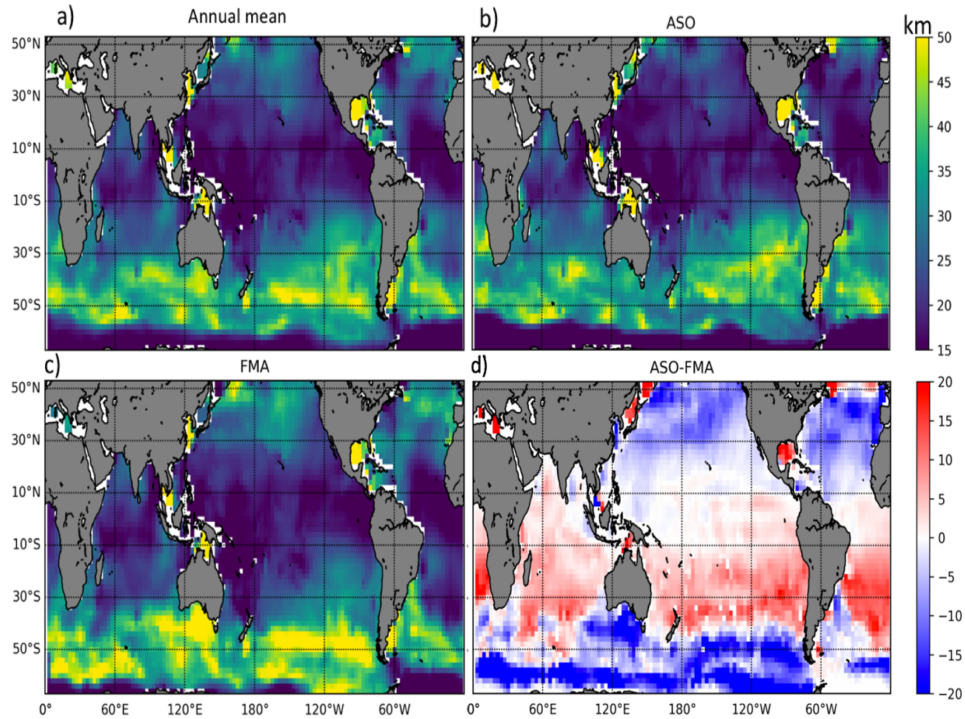
403 on the season and the oceanic region (see again Figure 7b). Many of these studies fur-
 404 ther show how energetic submesoscale fronts in winter can impact the mesoscale eddy
 405 field in spring and summer because of the time lag associated with the inverse KE cascade
 406 (see *Sasaki et al.* [2014]; *Qiu et al.* [2014]). Thus, MLIs at submesoscale in winter appear
 407 to provide an explanation of the puzzling seasonality of mesoscale KE (displaying a KE
 408 peak in spring/summer) observed in altimeter observations [*Zhai et al.*, 2008; *Sasaki et al.*,
 409 2014]. Numerical models also reveal a significant seasonality of the velocity wavenum-
 410 ber spectrum, displaying a k^{-2} slope in winter and k^{-3} slope in summer. These results are
 411 consistent with the *in-situ* data analysis of *Callies et al.* [2015] in the Gulf Stream re-
 412 gion, of *Qiu et al.* [2017] in the Western Pacific, as well as with the results from *Xu and*
 413 *Fu* [2012] and *Dufau et al.* [2016] based on a reanalysis of conventional altimeter observa-
 414 tions.

415 **4 Observational challenges using future satellite altimetry (SWOT)**

416 The theoretical and numerical results, of the last decade, on submesoscale balanced mo-
 417 tions and their impacts on mesoscale eddies, need to be confronted and confirmed by
 418 observations. Since these results emphasize a strong regionality and seasonality, obser-
 419 vations have to be global in space and continuous in time over several years. Only satel-
 420 lite altimetry can achieve this goal. Existing conventional radar altimetry has, however,
 421 two limitations. First, the instrument noise exceeds signal strength at wavelengths shorter
 422 than 50 – 70 km. Second, only one-dimensional SSH is profiled along the satellite ground
 423 tracks. To advance the observational capability, and in particular to capture a broader
 424 scale range of balanced motions, a wide-swath altimeter mission, SWOT, has been de-
 425 signed to observe SSH with a higher spatial resolution and in two dimensions [*Fu and Fer-*
 426 *rari*, 2008]. This is possible using the radar interferometry technique [*Fu and Ubelmann*,
 427 2014; *Rodríguez et al.*, 2018]. The SWOT resolution is expected to be about 15 km over
 428 68% of the ocean, assuming 2 m significant wave height, along a swath with a ~ 120 km
 429 width (see <https://swot.jpl.nasa.gov/mission.htm>).

434 However, before diagnosing balanced motions at scales smaller than 50–70 km using SWOT
 435 observations, several challenges have to be met. First, the measurement noise increases
 436 with significant height of surface waves and this noise is known to be seasonally and ge-
 437 ographically dependent. Second, at wavelengths shorter than ~ 100 km, the SSH signals
 438 of internal tides and internal gravity waves may become comparable to those of subme-
 439 soscale balanced motions. This entanglement of the balanced and wave motions is dis-
 440 cussed in more details in the next section. It leads to a complicated spatial and temporal
 441 variability of the scales of balanced motions resolvable by SWOT [*Qiu et al.*, 2018]. Using
 442 an OGCM with a high spatial resolution (similar to the one leading to Figure 3), *Wang*
 443 *et al.* [2019] studied the scales expected to be resolved by SWOT after taking into account
 444 the noise issues. Shown in Figure 10 are global maps of the minimum wavelengths, L_s ,
 445 possibly resolvable by SWOT. In the tropics, the measurement noise is generally the low-
 446 est owing to the small height of surface waves, leading to the highest resolution ($L_s < 20$
 447 km), which is also attributable to the shallow spectral slope of the SSH [*Xu and Fu*, 2012].
 448 In regions of the Southern Ocean with moderate mesoscale KE, the measurement noise
 449 is the worst owing to the large height of surface waves, which leads to the poorest reso-
 450 lution ($L_s \sim 40 - 50$ km). However, in other regions of the Southern Ocean with strong
 451 meso- and submesoscale eddies, such as downstream the Kerguelen Plateau, the resolu-
 452 tion is much better ($L_s < 30$ km). As shown in Figure 10d, during the winter seasons, the
 453 resolution is generally poorer than summer north of 40°S because of the effects of surface
 454 waves. The situation south of 40°S is different. During winter, the mesoscale energy is so
 455 high that the signal strength overcomes the increased noise, leading to higher resolution
 456 than summer.

457 In addition to the variability of the spatial resolution, the temporal sampling of SWOT
 458 is also challenging. Owing to the 120 km swath, it will take 21 days to map the world



430 **Figure 10.** The minimum wavelengths (in km), L_s , expected to be resolved by SWOT (a), in August-
 431 September-October (ASO) (b), in February-March-April (c). The seasonal change (ASO-FMA) is shown in
 432 panel (d). These wavelengths have been estimated using a numerical simulation (from Wang *et al.* [2019], ©
 433 American Meteorological Society. Used with permission)

459 oceans, with the number of repeat observations varying from 2 in the tropics to 6 at lati-
 460 tudes of 60°. Given the short time scales of the ocean variability at small scales, this tem-
 461 poral sampling poses another challenge to reconstruct coherent patterns of SSH over time.
 462 To meet this challenge, it is desirable to make use of high-resolution assimilative models
 463 guided by geophysical fluid dynamics argument [Ubelmann *et al.*, 2015], and also by an
 464 a priori knowledge of the relative contribution of balanced motions (BMs) and internal
 465 gravity waves (IGWs) (see Qiu *et al.* [2018] and Torres *et al.* [2018]). These last two stud-
 466 ies should help analyze the regionality and seasonality of observations at submesoscales.
 467 Given the global high-resolution measurements of SSH signals down to $O(15\text{km})$, the
 468 SWOT mission should provide us with unprecedented information about the evolution of
 469 small-mesoscale and submesoscale features and the possibility to reconstruct the upper
 470 ocean circulation such as relative vorticity and vertical velocity associated with balanced
 471 motions [Klein *et al.*, 2009; Qiu *et al.*, 2016]. By disentangling the SSH signals of BMs
 472 versus IGWs (see section 5 below), the SWOT-measured SSH data may also allow us to
 473 potentially explore interactions between the balanced and unbalanced motions.

474 **5 Balanced Motions (BMs) and Internal Gravity Waves (IGWs)**

475 As mentioned before, ocean currents with scales equal to or less than 300 km involve not
 476 only balanced motions (BMs) but also internal gravity waves (IGWs) whose properties
 477 significantly differ from BMs. IGWs include wind-forced near-inertial waves, with fre-

478 quencies close to f and coherent internal tides with diurnal and semi-diurnal frequencies
 479 [Müller *et al.*, 2015; Alford *et al.*, 2016]. IGWs also include a continuum of motions with
 480 frequencies higher than f and spatial scales smaller than 100 km (see Figure 11 panels i
 481 and ii). IGWs, unlike BMs, are characterized by a fast propagation and are mostly driven
 482 by weakly nonlinear interactions [Müller *et al.*, 2015], with almost zero PV (see Alford
 483 *et al.* [2016] for a review). These characteristics explain why, contrary to BMs, IGWs have
 484 almost no direct impact on vertical and horizontal advective fluxes of any quantity. On the
 485 other hand, IGWs are known to drive a large part of the ocean mixing through a direct
 486 KE cascade toward the smallest scales [Polzin and Lvov, 2011]. As a consequence, they
 487 trigger irreversible diffusive fluxes and therefore represent an important pathway for the
 488 route to dissipation of KE. However, studies of the last three years emphasize that charac-
 489 teristics of this pathway depend on how BMs and IGWs interact.

490 **5.1 Ocean Scale Interactions involving BMs and IGWs**

491 Although BMs and IGWs occupy distinct regions in the spectral space (see Figure 11),
 492 they do interact [Chereskin *et al.*, 2019]. Since Kunze [1985], many studies have revealed
 493 that IGW propagation is polarized by the sign of the relative vorticity and the sign of the
 494 stratification anomaly (or stretching) of mesoscale eddies [Kunze, 1985; Young and Jel-
 495 loul, 1997; Danioux *et al.*, 2011; Joyce *et al.*, 2013; Zaron and Egbert, 2014; Grisouard
 496 and Thomas, 2015; Ponte and Klein, 2015; Whitt and Thomas, 2015; Dunphy *et al.*, 2017;
 497 Thomas, 2017]. As a result, these waves may become trapped within anticyclonic eddies
 498 and expelled from cyclonic ones with their frequencies and wavenumbers significantly in-
 499 creasing during this process (see Whitt and Thomas [2015] for a short review). In other
 500 words, the scenario that emerges is that the scattering and dispersive impacts of BMs on
 501 IGWs may ultimately lead to intensified mixing in anticyclonic structures and reduced
 502 mixing in cyclonic ones which, in turn, modifies the OMT properties [Klein *et al.*, 2003].

503 Besides driving localized mixing, more recent studies suggest that the interactions between
 504 IGWs and BMs may stimulate submesoscale fronts and their associated vertical velocity
 505 field [Xie and Vanneste, 2015; Taylor and Straub, 2016; Wagner and Young, 2016; Barkan
 506 *et al.*, 2017; Thomas, 2017; Rocha *et al.*, 2018]. Thus, IGWs caught up in a balanced
 507 strain field may experience considerable modifications to their propagation direction and
 508 speed, leading to non-zero momentum and buoyancy fluxes associated with these waves
 509 [Thomas, 2017]. These fluxes represent an energy transfer from mesoscale KE to the wave
 510 PE, this energy being subsequently transferred to submesoscale fronts with high frequen-
 511 cies. Such mechanism, also called stimulated imbalance, leads to increase the vertical ve-
 512 locity field associated with submesoscale fronts and therefore the vertical advective fluxes
 513 of any quantities [Barkan *et al.*, 2017; Thomas, 2017; Rocha *et al.*, 2018]. These energy
 514 transfers are still not well understood and whether they can explain the energy observed
 515 in the region of "unbalanced motions" displayed in Figure 11, panel i, is unclear. Their
 516 confirmation by future studies will indicate whether high-frequency IGWs can lead, in ad-
 517 dition to irreversible mixing, to a substantial increase of vertical advective fluxes of any
 518 quantity [Su *et al.*, 2018].

519 In summary, understanding the interactions between BMs and IGWs, and the consequences
 520 on ocean mixing, is still in its infancy but is progressing quickly. Results obtained so far
 521 on this topic have been mostly obtained from numerical models. They need to be con-
 522 firmed or infirmed by observations. As a preliminary, the question is how to partition mo-
 523 tions into BMs and IGWs in the global ocean from observations.

524 **5.2 Partition of motions into BMs and IGWs in the Global Ocean**

525 BMs can be diagnosed from SSH for scales down to at least 100 km. Coherent tidal mo-
 526 tions have an impact on SSH at specific wavenumbers. These tidal peaks explain the shal-
 527 low SSH spectrum slope (much shallower than k^{-4}) found by Xu and Fu [2012] in low KE

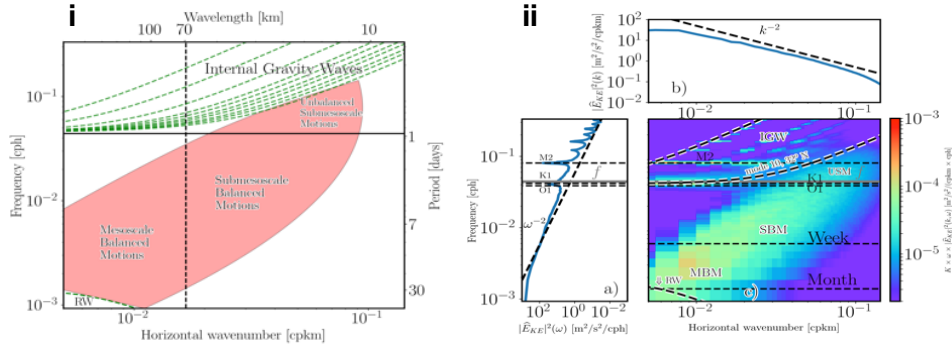
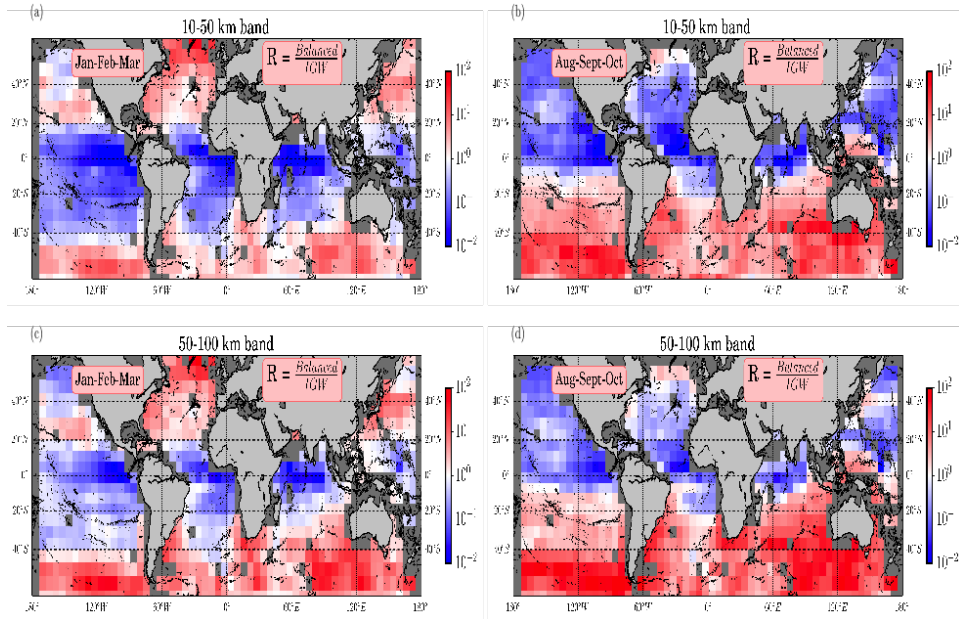


Figure 11. [From *Torres et al.* [2018]] i) Schematic spectrum displaying the multiple dynamical regimes: mesoscale and submesoscale balanced motions, "unbalanced motions" and IGWs. Additionally, the scheme shows the linear dispersion relations of the first ten baroclinic modes for IGWs (in green, upper part) and of baroclinic mode one for Rossby waves (in green, lower left corner). ii) Frequency-wavenumber spectra of KE ($E_{KE} [m^2/s^2/(cpkm \times cph)]$) corresponding to the Kuroshio-Extension region, in winter. The spectrum, estimated from a numerical simulation, is multiplied by k and ω . ii) a) frequency spectra. b) wavenumber spectra. and c) frequency-wavenumber spectra (from *Torres et al.* [2018]). Three horizontal bands with frequencies close to tidal (semi-diurnal and diurnal) and inertial frequencies span a larger range in the small scales band. Integrating this $\omega - k$ spectrum over the k -range or ω -range leads to the frequency spectrum a) or the wavenumber spectrum b) respectively.

regions (*Richman et al.* [2012], *Savage et al.* [2017a] and Joern Callies, personal communication). Tidal motions can be retrieved from long time series of SSH observations (that filter out mesoscale eddies) [*Egbert et al.*, 1994; *Stammer et al.*, 2014; *Ray and Mitchum*, 1997; *Ray and Zaron*, 2016]. Near-inertial waves have no impact on SSH [*Gill et al.*, 1974] but can be retrieved from surface drifters [*Lumpkin and Elipot*, 2010]. Diagnosing the IGW continuum with higher frequencies and higher wavenumbers (scales smaller than 100 km) from observations is still a challenge because of the strong entanglement of BMs and IGWs at these scales. Recent studies indicate this challenge may be partially met using satellite observations.

Using OGCMs with tides, several studies in the last three years have documented the spatial distribution of BMs and IGWs in the world ocean [*Rocha et al.*, 2016a; *Savage et al.*, 2017b,a] (see Figures 11 to 16 in *Savage et al.* [2017b]). *Qiu et al.* [2018] and *Torres et al.* [2018] have further analyzed when and where IGWs with scales smaller than 100 km have a dominant imprint on the surface fields observable from space. One important property exploited by *Qiu et al.* [2018] and *Torres et al.* [2018] (see also *Savage et al.* [2017a] and *Savage et al.* [2017b]) is that IGWs and BMs occupy two distinct regions in the $\omega - k$ spectral space, separated by the dispersion relation curve for the highest baroclinic mode of IGWs (see the schematic on Figure 11, panel i). The region above this curve (that includes frequencies equal to or higher than f) is associated with IGWs and exhibits discrete bands aligned with the linear dispersion relation of the different baroclinic modes, suggesting weakly nonlinear interactions (see Figure 11, panel ii) [*Rocha et al.*, 2016b; *Savage et al.*, 2017a; *Torres et al.*, 2018]. On the other hand, the region below the highest baroclinic mode is associated with BMs and has energy continuously spread out in the $\omega - k$ space, suggesting strong energy exchanges through nonlinear interactions (Figure 11, panel ii).

Qiu et al. [2018] and *Torres et al.* [2018] defined a criterion to discriminate BMs and IGWs for two scale ranges (10–50 km and 50–100 km). Their criterion R makes use of



563 **Figure 12.** Global maps of the ratio R (see below) for kinetic energy at the ocean surface (estimated from
 564 a numerical simulation): Top panels stand for submesoscale range (10-50 km); bottom panels stand for
 565 mesoscale range (50–100 km). Left panels are for January through March (winter in the Northern Hemisphere
 566 and summer in the Southern Hemisphere) and right panels are for August through September (summer in
 567 the Northern Hemisphere and winter in the Southern Hemisphere). For a given range of spatial scales, the
 568 variance above the dispersion relation curve for IGWs corresponding to the highest baroclinic mode has been
 569 associated with IGWs and the one below this curve associated with BMs. R is the ratio between the variance
 570 associated with BMs and that associated with IGWs: $R = \frac{BM\text{variance}}{IGW\text{variance}}$. So, for a given spatial-scale band, R
 571 > 1 means that the variability of the flow is explained by BMs; and $R < 1$ means the variability of the flow is
 572 explained by IGWs. These panels emphasize the strong seasonality of the partition of KE into IGWs and BMs
 573 for scales smaller than 100 km as well as the strong regional diversity and differences between Northern and
 574 Southern Hemispheres. (from *Torres et al.* [2018]).

577 a $\omega - k$ spectrum (see caption of Figure 12 for the definition of R). From the definition
 578 of R , BMs dominate for $R > 1$ and IGWs for $R < 1$. Based on 12000 $\omega - k$ spectra that
 579 cover the global ocean, their results highlight that IGWs dominate BMs in many regions
 580 (region in blue on Figure 12). Results emphasize, not only a strong seasonality (with BMs
 581 dominating in winter and IGWs in summer), but also a strong regional variability. These
 582 two studies further revealed that, in summer, the IGW impacts on SSH lead to a signifi-
 583 cant slope discontinuity on the SSH wavenumber spectrum, at scales smaller than 100 km,
 584 a discontinuity not observed on the KE spectrum. On the other hand, IGWs were found
 585 to have no impact on SST and SSS. These very different signatures of IGWs on SSH, KE,
 586 SST and SSS indicate that exploiting the synergy of using different satellite observations
 587 should help to discriminate IGWs and BMs in the global ocean [*Torres et al.*, 2018]. In
 588 that context, it is important to mention that, in addition to the SWOT mission, a future
 589 Wind and Current Mission (WaCM), still under development, aims to produce simultane-
 590 ous observations of wind stress and surface oceanic currents at high resolution [*Rodríguez*
 591 *et al.*, 2018]. The strong potential of WaCM will be to observe not only surface currents
 592 but also the wind work (i.e. the dot product of the wind stress and surface currents) and
 593 therefore to identify the wind-driven near-inertial motions that have no signature in SSH
 594 [*Gill et al.*, 1974].

6 Impact of Ocean Mesoscale/Submesoscale Turbulence on the Earth Climate

Balanced motions (including mesoscale and submesoscale motions) are now known to have a strong impact on the large-scale ocean circulation, the ocean biology and on the coupled ocean-atmosphere system, through the vertical and horizontal fluxes of any quantities. Recent studies, based on satellite altimeter products combined with *in-situ* observations and on results from numerical simulations within large domains at high resolution, have highlighted the ocean turbulence contribution to the transport of heat, mass, chemical constituents of seawater and air-sea interactions. In this section, we discuss some examples related to the impacts of this turbulence (that includes submesoscale fronts) on ocean dynamics and air-sea interactions. Impacts on ocean biology and carbon storage are discussed in recent review papers such as *Lévy et al.* [2012], *Mahadevan* [2016] and *McGillicuddy Jr* [2016].

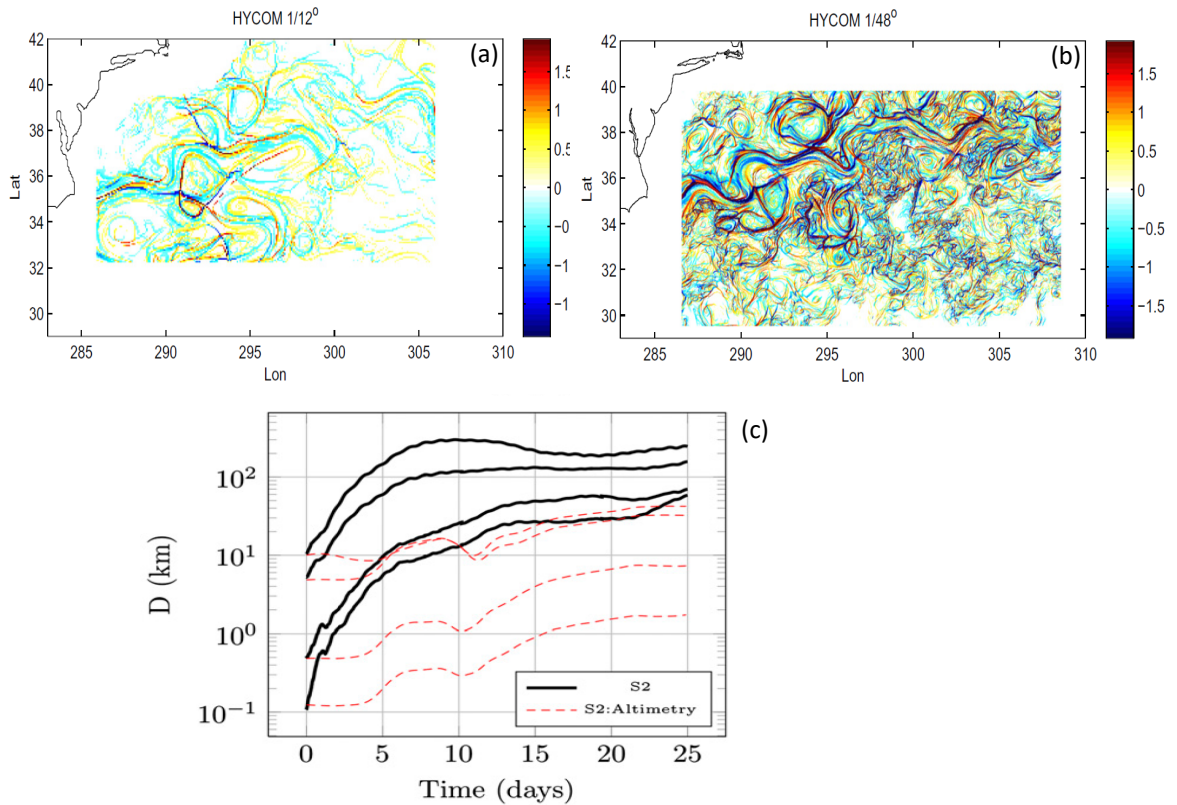
6.1 Stirring and Mixing Properties

The stretching (or strain) field and the Lagrangian accelerations associated with geostrophic eddies determine the properties of the dispersion of tracers and particles [*Hua and Klein*, 1998; *Lapeyre et al.*, 1999]. In GT, the k^{-3} KE spectrum slope implies that only by the largest eddies are responsible of the stretching of small-scale filaments. The tracer fluxes from large to small scales are associated with "non-local" scale interactions as the large scales control the small scales [*Scott*, 2006]. However, when the KE spectrum slope is in k^{-2} , such as when energetic submesoscale fronts/eddies are present, filament dynamics are controlled by all eddies (including submesoscale eddies). Such interactions are called "local" since small-scale filaments can be produced by the smallest eddies [*Scott*, 2006]. In that case the dispersion properties are much different from those driven by GT [*Scott*, 2006; *Özgökmen et al.*, 2012; *Foussard et al.*, 2017]. Differences between "local" and "non-local" properties are well highlighted by maps of Finite Size Lyapunov Exponents as displayed on Figures 13a,b (from *Haza et al.* [2012]). When submesoscale fronts/eddies are taken into account, FSLE are characterized by scales much smaller and magnitudes much larger (i.e. more intense stirring), than when submesoscale fronts/eddies are not taken into account.

Figure 13c (from *Poje et al.* [2014]) issued from the analysis of high resolution observations from surface drifters (that take into account submesoscale fronts and eddies) and SSH observations (that do not resolve submesoscale fronts and eddies) further quantifies the contribution of submesoscale fronts/eddies on the particle dispersion: particle dispersion is larger by at least one order of magnitude when estimated from high resolution observations that include submesoscales (black curves on Figure 13c) than with observations that do not include submesoscales (such as those from AVISO SSH, see the red dashed curves on Figure 13c).

6.2 Horizontal Heat Transport

Hausmann and Czaja [2012] analyzed the relationship between satellite microwave sea surface temperature (SST) and altimeter SSH observations. In regions of large SSH variability, SST and SSH mesoscale anomalies are nearly in-phase, involving intense warm-top anticyclones and cold-top cyclones. In quieter regions, weaker SST signatures are almost in quadrature with eddy SSH. These authors found that eddies flux heat pole-wards in the mixed-layer over a broad range of oceanic regimes. Magnitude of this heat transport, particularly significant in the Antarctic Circumpolar Current region, attains ~ 0.2 Petawatts, a value similar to that found by other studies using different observations, in particular the ARGO float dataset (see *Qiu and Chen* [2005] and *Dong et al.* [2014]), as well as studies using numerical simulations [*Lévy et al.*, 2010]. However, *Hausmann and Czaja* [2012] found that the pole-ward (equator-ward) propagation of warm anticyclones (cold cyclones) produces a much weaker pole-ward heat transport in the mixed

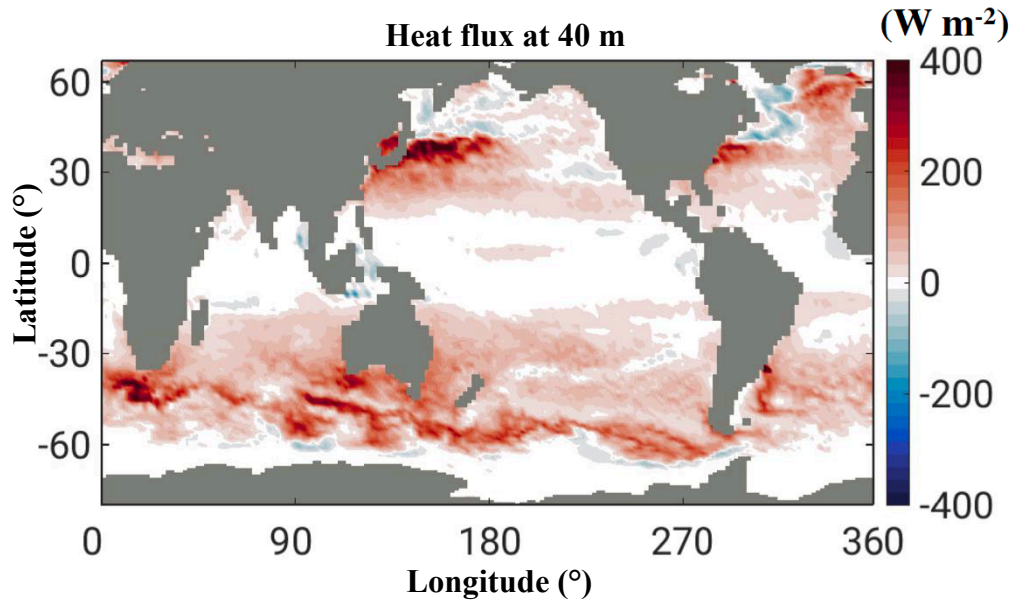


632 **Figure 13.** FSLE from a simulation without (a) and with submesoscales (b). The color panels indicate
 633 FSLE in day^{-1} . Blue colors show inflowing/stable trajectories from forward in time, and red colors out-
 634 flowing/unstable trajectories from backward in time particle advection. (from *Haza et al.* [2012], used with
 635 permission). (c) Separation distance of a particle pair as a function of time, $D(t)$, estimated in the Gulf of
 636 Mexico using (1) high resolution data from 300 drifters (black curves) and (2) low resolution AVISO SSH
 637 data (red). Dispersion is found to be 10-100 times larger when high resolution data are used (from *Poje et al.*
 638 [2014], used with permission).

652 layer than the horizontal fluxes resulting from the westward phase shift between SST and
 653 SSH fluctuations. In other words, the meridional heat transport is not so much due to in-
 654 dividual eddies transporting temperature anomalies, but it is principally due to horizon-
 655 tal heat fluxes resulting from the stirring of temperature anomalies by mesoscale eddies.
 656 This finding points to the importance of the phase shift between SSH and SST mesoscale
 657 anomalies for the estimation of the meridional heat fluxes. *Lévy et al.* [2010] further re-
 658 vealed that taking into account the impact of the submesoscale structures, in addition to
 659 that of mesoscale eddies, does not lead to a systematic increase of the total meridional
 660 heat transport. Rather, impacts of submesoscale structures lead to significantly decrease
 661 this transport in some regions and increase it in others (see their Figure 12).

662 6.3 Vertical heat transport

668 Submesoscale frontal dynamics are known to be characterized by $O(1)$ Rossby number
 669 and to capture most of the vertical velocity field in the upper ocean [*Klein and Lapeyre,*
 670 2009; *Mensa et al.,* 2013; *Sasaki et al.,* 2014; *Thompson et al.,* 2016; *McWilliams,* 2016].
 671 One consequence, revealed by *Hakim et al.* [2002] and confirmed by *Lapeyre and Klein*
 672 [2006] and *McWilliams et al.* [2009] (see also *Fox-Kemper et al.* [2008, 2011]), is that

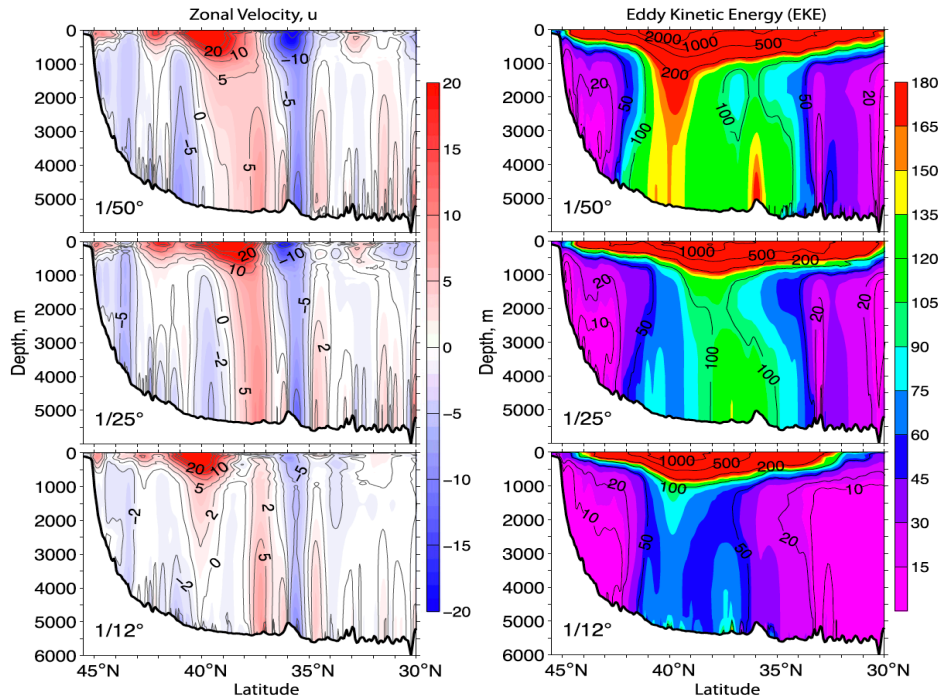


663 **Figure 14.** Global patterns of vertical heat transport (estimated from a numerical simulation) explained
 664 by submesoscales (<50 km) in winter (January-March for the Northern Hemisphere and July-September for
 665 the Southern Hemisphere). Values are spatially smoothed over $3^\circ \times 3^\circ$ square boxes; positive values indicate
 666 upward. In most area of mid-latitudes, vertical heat transport at submesoscales is $\sim 20 - 200 \text{ W/m}^2$ and is
 667 systematically upwards (adapted from *Su et al.* [2018], used with permission).

673 these submesoscale fronts are associated with positive vertical heat fluxes, i.e. up-gradient
 674 (from deep cold waters to surface warm waters) and not down-gradient. This adiabatic
 675 property has been highlighted in a recent paper by *Su et al.* [2018] using an OGCM at
 676 unprecedented high spatial resolution (2 km in the horizontal and 90 vertical levels). Re-
 677 sults indicate that upper-ocean submesoscale turbulence produces a systematically upward
 678 heat transport that is 5 to 10 times larger than the vertical heat transport explained by
 679 mesoscale eddies! Wintertime magnitudes of these submesoscale heat fluxes are up to 200
 680 W/m^2 for mid-latitudes (when averaged over 3 months and in boxes of 300 km size, see
 681 Figure 14). These vertical heat fluxes warm the sea surface by up to 0.3°C annually and
 682 produce an upward annual-mean air-sea heat flux anomaly of $4-10 \text{ W/m}^2$ at mid-latitudes
 683 [*Su et al.*, 2018]. Such results indicate that submesoscale balanced motions associated with
 684 submesoscale frontal structures are critical to the vertical transport of heat between the
 685 ocean interior and the atmosphere, and are thus a key component of the Earth's climate.
 686 Noting that submesoscale fronts are pre-conditioned by mesoscale eddies, the results from
 687 *Su et al.* [*Su et al.*, 2018] further highlight the impacts of the ocean scale interactions on
 688 the Earth Climate.

689 **6.4 Impact of Submesoscale Fronts on the Large-scale Ocean Circulation**

693 The impact of submesoscale frontal physics on the large-scale ocean circulation has been
 694 examined by *Lévy et al.* [2010] and *Chassignet et al.* [2017]. To test this impact, these
 695 authors used several numerical models at a basin-scale, each one with a different spatial
 696 resolution. After a reasonable spin-up period (10–20 years), the large-scale ocean circula-
 697 tion and the mean structure of the ventilated thermocline strongly differ when the res-
 698 olution increased from 10 km to 2 km (which highlights the impact of submesoscales).
 699 Changes involve the emergence of a denser and more energetic eddy population at the 2



690 **Figure 15.** Vertical distribution of the modeled (left) zonal velocity (cm/s) and (right) eddy kinetic energy
 691 (cm^2/s^2) along $55^\circ W$ for the $1/50^\circ$, $1/25^\circ$, and $1/12^\circ$ numerical simulations (from Chassignet *et al.* [2017],
 692 © American Meteorological Society. Used with permission).

700 km-resolution, occupying most of the basin and sustained by submesoscale physics. Tak-
 701 ing into account submesoscale dynamics lead to "regional" and "remote" effects. "Re-
 702 gional" effects occur through the inverse KE cascade that strongly intensifies zonal jets
 703 such as in the Gulf Stream region. This intensification subsequently leads to isopycnals
 704 steepening (through the thermal wind balance), which significantly counter-balances and
 705 locally overcomes the eddy-driven heat transport that tends to flatten isopycnals [Lévy
 706 *et al.*, 2010]. Chassignet *et al.* [2017] further note that, when the spatial resolution is in-
 707 creased, the representation of the Gulf Stream penetration and associated recirculating
 708 gyres changes from unrealistic (in terms of comparison with observations) and
 709 that the penetration into the deep ocean drastically increases (see Figure 15). "Remote" ef-
 710 fects occur through the resulting general equilibration of the main thermocline that shifts
 711 zonal jets at mid-latitudes southward by a few degrees, significantly altering the shape
 712 and position of the gyres. Consequence is that the deep convection in high latitudes is
 713 reduced, leading to a significant modification of the meridional overturning circulation.
 714 Thus, results from Lévy *et al.* [2010] and Chassignet *et al.* [2017] emphasize that the im-
 715 pact of submesoscale fronts on the mean circulation and mean transport at a basin scale
 716 cannot be ignored anymore. There is a need to repeat these two numerical experiments in
 717 larger domains with an even higher spatial resolution (Joern Callies, personal communica-
 718 tion), in particular on the vertical, using the coming exa-scale computers.

719 6.5 Air-Sea Interaction

720 Chelton *et al.* [2004] discovered a remarkably strong positive correlation between surface
 721 winds and SST at mesoscale (i.e. 100–300 km) using a combination of radar scatterome-
 722 ters and SST observations. As shown later by Frenger *et al.* [2013], mesoscale eddies are

723 characterized by a positive correlation between SST, SSH, cloudiness and precipitation
724 rate. Similar correlations were found between air-sea heat fluxes and SST [Byrne *et al.*,
725 2015; Ma *et al.*, 2015; Bôas *et al.*, 2015]. An arising question concerns the impact of
726 OMT at the scale of the atmospheric storm track (i.e. $O(5000-10000\text{ km})$). Ma *et al.* [2015]
727 and Foussard *et al.* [2019] showed that increased air-sea heat fluxes at the ocean surface,
728 due to oceanic eddies, could lead to a non-local response associated with a modification
729 of the atmospheric circulation far from the oceanic eddying region.

730 In parallel, using numerical models with spatial resolution accounting for scales as small
731 as 50 km, Minobe *et al.* [2008] showed that local SST fronts in the Gulf Stream could
732 impact the entire troposphere. These authors found a conspicuous signal in their atmo-
733 spheric general circulation model, indicating a wind convergence over the warm flank of
734 the oceanic front up to 12 km in altitude (i.e. close to the tropopause). One important
735 characteristic is that the wind convergence was found to be proportional to the SST Lapla-
736 cian (a second order derivative that involves small scales). This sensitivity to small scales
737 explains why past numerical models, with lower resolution, were unable to represent such
738 dynamics [Bryan *et al.*, 2010]. Since then, numerous studies with higher spatial resolution
739 have highlighted the importance of such SST gradients, with scales down to the subme-
740 soscales, for the tropospheric storm tracks [Nakamura *et al.*, 2008; Deremble *et al.*, 2012;
741 Foussard *et al.*, 2019]. These results have led to a renewed interest in understanding the
742 role played by SST anomalies at scales down to 5–10 km in atmosphere dynamics.

743 Although the ocean current magnitude is much smaller than the atmospheric wind speed,
744 a large number of numerical studies, at least in the last two decades, have shown that
745 oceanic currents at mesoscales and submesoscales can also significantly impact the wind
746 stress. In terms of ocean dynamics, the resulting effects on the wind work lead to a net
747 KE transfer from the ocean to the atmosphere. This transfer corresponds to a decay of
748 almost 30% of the ocean KE at mesoscale at mid-latitudes [Eden and Dietze, 2009] and
749 less than 20% for oceanic submesoscales [Renault *et al.*, 2018]. In terms of atmospheric
750 dynamics, the wind stress curl and divergence resulting from the ocean current impacts
751 should affect the vertical velocity in the atmosphere. A recent in-situ experiment has been
752 carried out in the Gulf of Mexico using a Doppler Scatterometer to observe simultane-
753 ously the surface currents and wind stress at very high resolution ($\sim 2.5\text{ km}$). The results
754 reveal and confirm the strong correlation between the wind stress curl and the relative
755 vorticity associated with oceanic submesoscales (Ernesto Rodriguez, personal communi-
756 cation). Magnitude of the wind stress curl is such that the wind divergence in the atmo-
757 sphere is one order of magnitude larger than found by Minobe *et al.* [2008].

758 These results further confirm that oceanic mesoscale eddies and submesoscales structures
759 can significantly impact the atmospheric boundary layer and the whole troposphere. There
760 is still some work to do to further quantify these impacts and the consequences on the
761 atmospheric storm tracks.

762 **7 Discussion and Conclusion**

763 Analysis of altimeter observations collected in the last 25 years and results obtained from
764 OGCMs with high spatial resolution emphasize that all the oceans are fully turbulent, in-
765 volving a broad range of scales from at least 2 km to 5000 km. All these scales are now
766 known to strongly interact, leading to significant energy exchanges between scales, in par-
767 ticular in the upper ocean. Resulting ocean scale interactions impact the Earth climate in
768 counter-intuitive ways. For instance, the smallest scales render mesoscale eddies more co-
769 herent with a longer lifetime and can also trigger significant up-gradient and not down-
770 gradient vertical fluxes of any quantity. A better understanding of the internal gravity
771 waves impacts may lead to a more complex vision depending on how much they interact
772 with balanced motions. Overall, results highlight that the oceanic fluid is much less dia-
773 batic and much more inertial than thought 25 years ago (i.e. again with fluxes much less

774 controlled by diffusivity or viscosity and more by nonlinear interactions that lead to re-
775 versible up and down gradient fluxes). Numerous studies now emphasize that these ocean
776 scale interactions are crucial for the ocean's kinetic energy budget, the meridional heat
777 transport, the air-sea interactions and more generally for the Earth climate.

778 Running numerical models with high resolution is a powerful approach to assess ocean
779 scale interactions, but only when they are performed with the highest spatial resolution
780 (down to at least 1 km) and on a global scale in order to take into account, both, the "lo-
781 cal" and "non-local" interactions. This strategy is the only one capable to assess the wealth
782 of ocean scale interactions over a broad range of scales. Such ocean numerical models
783 as well as atmosphere-ocean coupled models with similar resolutions can be run on the
784 present peta-scale computers and the coming exa-scale computers. Future numerical mod-
785 els, with a higher resolution than presently considered, will certainly challenge the re-
786 sults presented in this paper, by revealing new and unsuspected impacts of smaller scales
787 presently unresolved. These models will undoubtedly improve our understanding of the
788 ocean engine.

789 Numerical findings need however to be confirmed or infirmed by high-resolution obser-
790 vations on a global scale and over several years, as already pointed out by Carl Wunsch
791 in 2010. As emphasized in this paper, balanced motions and internal gravity waves have
792 different impacts in terms of fluxes on the KE budget, which points to the need to dis-
793 criminate them from observations. In that respect, future wide-swath altimeter missions,
794 such as the SWOT mission [*Fu and Ferrari, 2008*], will be critical to make major ad-
795 vances. These observations are the only ones capable to diagnose correctly balanced mo-
796 tions down to scales of 30–50 km. However, these future SSH observations will have to
797 be combined with existing satellite observations as well as with those from missions un-
798 der development to retrieve other IGWs. The latter missions include WaCM [*Rodríguez*
799 *et al., 2018*], already mentioned, that will observe simultaneously the wind stress and
800 oceanic currents at very high resolution, and therefore give access to near-inertial waves
801 and smaller IGWs. They also include other missions such as the Surface KInematic Mon-
802 itoring mission (SKIM, *Ardhuin et al. [2018]*) and the Wavemill mission [*Martin et al.,*
803 *2016*] aiming to observe surface currents with high resolution. An optimal strategy to bet-
804 ter capture the subtleties of ocean turbulence would be to exploit the synergy of analyzing
805 all these satellite observations in combination with *in situ* data on a global scale, such as
806 the ones collected by surface drifters [*Lumpkin et al., 2017*] and ARGO floats [*Le Traon,*
807 *2013*] deployed in all oceans.

808 The importance, for the Earth climate, of fully taking into account the ocean scale inter-
809 actions is further emphasized by recent geophysical studies on the Earth atmosphere and
810 oceans. The Earth atmosphere involves cyclones and anticyclones (although with larger
811 scales than in the oceans) that strongly interact, the so-called atmospheric storm-tracks.
812 However, if geophysical turbulence refers to an inverse KE cascade over a broad inertial
813 range (defined as the scale range between the eddy source scale and the scale of the most
814 energetic eddies), the atmosphere is found much less turbulent than the oceans [*Jansen*
815 *and Ferrari, 2012*]. The atmosphere is indeed characterized by an inverse KE cascade over
816 a very small inertial range compared to the oceans [*Schneider and Walker, 2006; Merlis*
817 *and Schneider, 2009*]. Scales of the atmospheric cyclones and anticyclones are close to
818 their source scales (scales of the baroclinic instability). On the other hand, as pointed out
819 several times in this paper, the ocean mesoscale turbulence is characterized by an inverse
820 KE cascade over a broad inertial range. [*Hua and Haidvogel, 1986; Hua et al., 1998*]. The
821 consequence, as discussed by *Jansen and Ferrari [2012]*, is that the atmospheric response
822 to external forcings is much faster and much less inertial than the ocean response, which
823 should impact the dynamics of the coupled ocean-atmosphere system. These differences
824 between the ocean and atmosphere turbulent properties emphasize the importance of the
825 future developments on ocean scale interactions for studies of climate and climate change
826 [*Jansen and Ferrari, 2012*].

Acknowledgments

We dedicate this study to our colleague and friend Bach Lien Hua who was the first woman to give a Lorenz Conference (in 2006) and who made so many significant and insightful contributions to the understanding of oceanic turbulence. We thank the two reviewers for their constructive comments and in particular Eric Chassignet for his advices during the revision process. We also thank Jinbo Wang for his insightful comments. This study was carried out at the Jet Propulsion Laboratory, California Institute of Technology, under contract with the National Aeronautics and Space Administration (NASA), at the Laboratoire de Météorologie Dynamique and at the Courant Institute. P.K. is supported by a NASA Senior Fellowship and the SWOT mission. G.L. is supported by the CNES-SWOT mission. L.S. is a JPL JVSREP affiliate and is supported by a joint CNES–Région Bretagne doctoral grant. B.Q. and L.L.F. acknowledge support from the NASA SWOT mission (NNX16AH66G). H. T. and D.M. are supported by NASA Physical Oceanography (PO) and Modeling, Analysis, and Prediction (MAP) Programs. Z. S. has been supported from NASA NPP postdoc fellowship and NASA grant NNX15AG42G. This work is partly funded by CNES (OSTST–OSIW grant) and the Laboratoire d’Excellence LabexMER (ANR–10–LABX–19). Data used in this paper can be found in <https://science.jpl.nasa.gov/projects/ECCO-IcES/>

References

- Alford, M. H., J. A. MacKinnon, H. L. Simmons, and J. D. Nash (2016), Near-inertial internal gravity waves in the ocean, *Annual review of marine science*, *8*, 95–123.
- Arbic, B. K., R. B. Scott, G. R. Flierl, A. J. Morten, J. G. Richman, and J. F. Shriver (2012), Nonlinear cascades of surface oceanic geostrophic kinetic energy in the frequency domain, *Journal of Physical Oceanography*, *42*(9), 1577–1600.
- Arbic, B. K., K. L. Polzin, R. B. Scott, J. G. Richman, and J. F. Shriver (2013), On eddy viscosity, energy cascades, and the horizontal resolution of gridded satellite altimeter products, *Journal of Physical Oceanography*, *43*(2), 283–300.
- Ardhuin, F., Y. Aksenov, A. Benetazzo, L. Bertino, P. Brandt, A. Caube, et al. (2018), Measuring currents, ice drift, and waves from space: The sea surface kinematics multi-scale monitoring (skim) concept, *Ocean Science*, *14*, 337–354.
- Aref, H. (1984), Stirring by chaotic advection, *Journal of Fluid Mechanics*, *143*, 1–21.
- Barkan, R., K. B. Winters, and J. C. McWilliams (2017), Stimulated imbalance and the enhancement of eddy kinetic energy dissipation by internal waves, *Journal of Physical Oceanography*, *47*(1), 181–198.
- Blumen, W. (1978), Uniform potential vorticity flow: Part i. theory of wave interactions and two-dimensional turbulence, *Journal of the Atmospheric Sciences*, *35*(5), 774–783.
- Bôas, A. V., O. Sato, A. Chaigneau, and G. Castelão (2015), The signature of mesoscale eddies on the air-sea turbulent heat fluxes in the south atlantic ocean, *Geophysical Research Letters*, *42*(6), 1856–1862.
- Boccaletti, G., R. Ferrari, and B. Fox-Kemper (2007), Mixed layer instabilities and restratification, *Journal of Physical Oceanography*, *37*(9), 2228–2250.
- Bryan, F. O., R. Tomas, J. M. Dennis, D. B. Chelton, N. G. Loeb, and J. L. McClean (2010), Frontal scale air–sea interaction in high-resolution coupled climate models, *Journal of Climate*, *23*(23), 6277–6291.
- Byrne, D., L. Papritz, I. Frenger, M. Münnich, and N. Gruber (2015), Atmospheric response to mesoscale sea surface temperature anomalies: Assessment of mechanisms and coupling strength in a high-resolution coupled model over the south atlantic, *Journal of the Atmospheric Sciences*, *72*(5), 1872–1890.
- Callies, J., R. Ferrari, J. M. Klymak, and J. Gula (2015), Seasonality in submesoscale turbulence, *Nature communications*, *6*, 6862.
- Callies, J., G. Flierl, R. Ferrari, and B. Fox-Kemper (2016), The role of mixed-layer instabilities in submesoscale turbulence, *Journal of Fluid Mechanics*, *788*, 5–41.

- 879 Capet, X., P. Klein, B. Hua, G. Lapeyre, and J. McWilliams (2008), Surface kinetic and
880 potential energy transfer in sqg dynamics, *J. Fluid Mech*, *604*, 165–174.
- 881 Capet, X., G. Roulet, P. Klein, and G. Maze (2016), Intensification of upper-ocean
882 submesoscale turbulence through charney baroclinic instability, *Journal of Physical*
883 *Oceanography*, *46*(11), 3365–3384.
- 884 Charney, J. G. (1947), The dynamics of long waves in a baroclinic westerly current, *Jour-*
885 *nal of Meteorology*, *4*(5), 136–162.
- 886 Charney, J. G. (1971), Geostrophic turbulence, *Journal of the Atmospheric Sciences*, *28*(6),
887 1087–1095.
- 888 Chassignet, E., , and X. Xu (2017), Impact of horizontal resolution (1/12 $\hat{\text{A}}$ to 1/50 $\hat{\text{A}}$) on
889 gulf stream separation, penetration, and variability, *Journal of Physical Oceanography*,
890 *47*, 1999–2021.
- 891 Chassignet, E., A. Pascual, J. Tintore, and J. Verron (2018), *New Frontiers in Operational*
892 *Oceanography*, GODAE OceanView.
- 893 Chelton, D. B., M. G. Schlax, M. H. Freilich, and R. F. Milliff (2004), Satellite measure-
894 ments reveal persistent small-scale features in ocean winds, *science*, *303*(5660), 978–
895 983.
- 896 Chelton, D. B., M. G. Schlax, and R. M. Samelson (2011), Global observations of nonlin-
897 ear mesoscale eddies, *Progress in Oceanography*, *91*(2), 167–216.
- 898 Chereskin, T., C. Rocha, S. Gille, D. Menemenlis, and M. Passare (2019), Characterizing
899 the transition from balanced to unbalanced motions in the southern california current,
900 *Journal of Geophysical Research*.
- 901 Danioux, E., P. Klein, M. W. Hecht, N. Komori, G. Roulet, and S. Le Gentil (2011),
902 Emergence of wind-driven near-inertial waves in the deep ocean triggered by small-
903 scale eddy vorticity structures, *Journal of Physical Oceanography*, *41*(7), 1297–1307.
- 904 Deremble, B., G. Lapeyre, and M. Ghil (2012), Atmospheric dynamics triggered by an
905 oceanic sst front in a moist quasigeostrophic model, *Journal of the Atmospheric Sci-*
906 *ences*, *69*(5), 1617–1632.
- 907 Dong, C., J. C. McWilliams, Y. Liu, and D. Chen (2014), Global heat and salt transports
908 by eddy movement, *Nature communications*, *5*, 3294.
- 909 d’Ovidio, F., S. DeMonte, S. Alvain, Y. Dandonneau, and M. Levy (2010), Fluid dynam-
910 ical niches of phytoplankton types, *Proceeding of the National Academy of Sciences*, p.
911 doi/10.1073/pnas.1004620107.
- 912 Dufau, C., M. Orszynowicz, G. Dibarboure, R. Morrow, and P.-Y. Le Traon (2016),
913 Mesoscale resolution capability of altimetry: Present and future, *Journal of Geophysi-*
914 *cal Research: Oceans*, *121*(7), 4910–4927.
- 915 Dunphy, M., A. L. Ponte, P. Klein, and S. Le Gentil (2017), Low-mode internal tide prop-
916 agation in a turbulent eddy field, *Journal of Physical Oceanography*, *47*(3), 649–665.
- 917 Eden, C., and H. Dietze (2009), Effects of mesoscale eddy/wind interactions on biological
918 new production and eddy kinetic energy, *Journal of Geophysical Research: Oceans*, *114*,
919 C05,023.
- 920 Egbert, G. D., A. F. Bennett, and M. G. Foreman (1994), Topex/poseidon tides estimated
921 using a global inverse model, *Journal of Geophysical Research: Oceans*, *99*(C12),
922 24,821–24,852.
- 923 Ferrari, R. (2011), A frontal challenge for climate models, *Science*, *332*(6027), 316–317.
- 924 Ferrari, R., and C. Wunsch (2009), Ocean circulation kinetic energy: Reservoirs, sources,
925 and sinks, *Annual Review of Fluid Mechanics*, *41*.
- 926 Foussard, A., S. Berti, X. Perrot, and G. Lapeyre (2017), Relative dispersion in general-
927 ized two-dimensional turbulence, *Journal of Fluid Mechanics*, *821*, 358–383.
- 928 Foussard, A., G. Lapeyre, and P. R (2019), Storm tracks response to oceanic eddies in
929 idealized atmospheric simulations, *Journal of Climate*, *32*, 445–463.
- 930 Fox-Kemper, B., R. Ferrari, and R. Hallberg (2008), Parameterization of mixed layer ed-
931 dies. part i: Theory and diagnosis, *Journal of Physical Oceanography*, *38*(6), 1145–
932 1165.

- 933 Fox-Kemper, B., G. Danabasoglu, R. Ferrari, S. Griffies, R. Hallberg, M. Holland,
934 M. Maltrud, S. Peacock, and B. Samuels (2011), Parameterization of mixed layer ed-
935 dies. iii: Implementation and impact in global ocean climate simulations, *Ocean Mod-*
936 *elling*, 39(1-2), 61–78.
- 937 Frenger, I., N. Gruber, R. Knutti, and M. Münnich (2013), Imprint of southern ocean ed-
938 dies on winds, clouds and rainfall, *Nature geoscience*, 6(8), 608.
- 939 Fu, L.-L. (1983), On the wave number spectrum of oceanic mesoscale variability observed
940 by the seasat altimeter, *Journal of Geophysical Research: Oceans*, 88(C7), 4331–4341.
- 941 Fu, L.-L. (2009), Pattern and velocity of propagation of the global ocean eddy variability,
942 *Journal of Geophysical Research: Oceans*, 114(C11).
- 943 Fu, L.-L., and R. Ferrari (2008), Observing oceanic submesoscale processes from space,
944 *Eos, Transactions American Geophysical Union*, 89(48), 488–488.
- 945 Fu, L.-L., and G. R. Flierl (1980), Nonlinear energy and enstrophy transfers in a realisti-
946 cally stratified ocean., *Dyn. Atmos. Oceans*, 4, 219–246.
- 947 Fu, L.-L., and R. D. Smith (1996), Global ocean circulation from satellite altimetry and
948 high-resolution computer simulation, *Bulletin of the American Meteorological Society*,
949 77(11), 2625–2636.
- 950 Fu, L.-L., and C. Ubelmann (2014), On the transition from profile altimeter to swath al-
951 timeter for observing global ocean surface topography, *Journal of Atmospheric and*
952 *Oceanic Technology*, 31, 560–568.
- 953 Garrett, C. (1983), On the initial streakiness of a dispersing tracer in two- and three-
954 dimensional turbulence, *Dynamics of Atmospheres and Oceans*, 7, 265–277.
- 955 Gaultier, L., J. Verron, J. Brankart, O. Titaud, and P. Brasseur (2012), On the inversion of
956 submesoscale tracer fields to estimate the surface ocean circulation, *Journal of Marine*
957 *Systems*, p. doi:10.1016/j.jmarsys.2012.02.014.
- 958 Gill, A., J. Green, and A. Simmons (1974), Energy partition in the large-scale ocean cir-
959 culation and the production of mid-ocean eddies, *Deep-Sea Res*, 21(7), 499–528.
- 960 Grisouard, N., and L. N. Thomas (2015), Critical and near-critical reflections of near-
961 inertial waves off the sea surface at ocean fronts, *Journal of Fluid Mechanics*, 765, 273–
962 302.
- 963 Hakim, G. J., C. Snyder, and D. J. Muraki (2002), A new surface model for cyclone–
964 anticyclone asymmetry, *Journal of the atmospheric sciences*, 59(16), 2405–2420.
- 965 Hausmann, U., and A. Czaja (2012), The observed signature of mesoscale eddies in
966 sea surface temperature and the associated heat transport, *Deep Sea Research Part I:*
967 *Oceanographic Research Papers*, 70, 60–72.
- 968 Haza, A., T. Ozgokmen, A. Griffa, Z. Garraffo, and L. Piterbarg (2012), Parameterization
969 of particle transport at submesoscales in the gulf stream region using lagrangian sub-
970 gridscale models, *Ocean Modelling*, 42, 31–49.
- 971 Held, I. M., R. T. Pierrehumbert, S. T. Garner, and K. L. Swanson (1995), Surface quasi-
972 geostrophic dynamics, *Journal of Fluid Mechanics*, 282, 1–20.
- 973 Hoskins, B. (1976), Baroclinic waves and frontogenesis part i: Introduction and eady
974 waves, *Quarterly Journal of the Royal Meteorological Society*, 102(431), 103–122.
- 975 Hua, B., and D. Haidvogel (1986), Numerical simulations of the vertical structure of
976 quasi-geostrophic turbulence, *Journal of the atmospheric sciences*, 43(23), 2923–2936.
- 977 Hua, B., J. McWilliams, and P. Klein (1998), Lagrangian accelerations in geostrophic tur-
978 bulence, *Journal of Fluid Mechanics*, 366, 87–108.
- 979 Hua, B. L., and P. Klein (1998), An exact criterion for the stirring properties of nearly
980 two-dimensional turbulence, *Physica D*, 113, 98–110.
- 981 Hua, B.-L., J. C. McWilliams, and B. Owens (1985), An objective analysis of the poly-
982 mode local dynamics experiment. part ii: Streamfunction and potential vorticity fields
983 during the extensive period, *Journal of Physical Oceanography*, 16, 506–522.
- 984 Hurlburt, H. E., and P. J. Hogan (2000), Impact of 1/8 to 1/64 resolution on gulf stream
985 model–data comparisons in basin-scale subtropical atlantic ocean models, *Dynamics of*
986 *Atmospheres and Oceans*, 32(3-4), 283–329.

- 987 Jansen, M., and R. Ferrari (2012), Macroturbulent equilibration in a thermally forced
988 primitive equation system, *Journal of the Atmospheric Sciences*, *69*(2), 695–713.
- 989 Joyce, T., J. Toole, P. Klein, and L. Thomas (2013), A near-inertial mode observed
990 within a gulf stream warm-core ring, *Journal of Geophysical Research*, *118*(c3),
991 doi:10.1002/jgrc.20,141.
- 992 Juckes, M. (1994), Quasigeostrophic dynamics of the tropopause, *Journal of the Atmo-*
993 *spheric Sciences*, *51*(19), 2756–2768.
- 994 Klein, P., and G. Lapeyre (2009), The oceanic vertical pump induced by mesoscale and
995 submesoscale turbulence, *Annual review of marine science*, *1*, 351–375.
- 996 Klein, P., B.-L. Hua, and X. Carton (2003), Emergence of cyclonic structures due to the
997 interactions of near-inertial oscillations with mesoscale eddies, *Quarterly Journal of the*
998 *Royal Meteorological Society*, *129*, 1–20.
- 999 Klein, P., B. L. Hua, G. Lapeyre, X. Capet, S. Le Gentil, and H. Sasaki (2008), Upper
1000 ocean turbulence from high-resolution 3d simulations, *Journal of Physical Oceanogra-*
1001 *phy*, *38*(8), 1748–1763.
- 1002 Klein, P., J. Isern-Fontanet, G. Lapeyre, G. Roullet, E. Danioux, B. Chapron, S. Le Gen-
1003 til, and H. Sasaki (2009), Diagnosis of vertical velocities in the upper ocean from high
1004 resolution sea surface height, *Geophysical Research Letters*, *36*, L12,603.
- 1005 Kunze, E. (1985), Near-inertial wave propagation in geostrophic shear, *Journal of Physical*
1006 *Oceanography*, *15*(5), 544–565.
- 1007 LaCasce, J. (2012), Surface quasigeostrophic solutions and baroclinic modes with expo-
1008 nential stratification, *Journal of Physical Oceanography*, *42*, 549–580.
- 1009 LaCasce, J., and A. Mahadevan (2006), Estimating subsurface horizontal and vertical ve-
1010 locities from sea-surface temperature, *Journal of Marine Research*, *64*(5), 695–721.
- 1011 Lapeyre, G. (2002), Characterization of finite-time lyapunov exponents and vectors in two-
1012 dimensional turbulence, *Chaos: An Interdisciplinary Journal of Nonlinear Science*, *12*(3),
1013 688–698.
- 1014 Lapeyre, G. (2017), Surface quasi-geostrophy, *Fluids*, *2*(1), 7.
- 1015 Lapeyre, G., and P. Klein (2006), Dynamics of the upper oceanic layers in terms of sur-
1016 face quasigeostrophy theory, *Journal of physical oceanography*, *36*(2), 165–176.
- 1017 Lapeyre, G., P. Klein, and B. Hua (1999), Does the tracer gradient vector align with the
1018 strain eigenvectors in 2d turbulence?, *Physics of fluids*, *11*(12), 3729–3737.
- 1019 Lapeyre, G., B. Hua, and P. Klein (2001), Dynamics of the orientation of active and pas-
1020 sive scalars in two-dimensional turbulence, *Physics of Fluids*, *13*(1), 251–264.
- 1021 Lapeyre, G., P. Klein, and B.-L. Hua (2006), Oceanic restratification forced by surface
1022 frontogenesis, *Journal of physical oceanography*, *36*(2), 1577–1590.
- 1023 Le Traon, P.-Y. (2013), From satellite altimetry to argo and operational oceanography:
1024 three revolutions in oceanography, *Ocean Science*, *9*, 901–915.
- 1025 Le Traon, P.-Y., P. Klein, B. L. Hua, and G. Dibarboure (2008), Do altimeter wavenumber
1026 spectra agree with the interior or surface quasigeostrophic theory?, *Journal of Physical*
1027 *Oceanography*, *38*(5), 1137–1142.
- 1028 Ledwell, J. R., A. J. Watson, and C. S. Law (1993), Evidence for slow mixing across the
1029 pycnocline from an open-ocean tracer-release experiment, *Nature*, *364*(6439), 701.
- 1030 Lévy, M., P. Klein, and A.-M. Treguier (2001), Impact of sub-mesoscale physics on pro-
1031 duction and subduction of phytoplankton in an oligotrophic regime, *Journal of marine*
1032 *research*, *59*(4), 535–565.
- 1033 Lévy, M., P. Klein, A.-M. Tréguier, D. Iovino, G. Madec, S. Masson, and K. Takahashi
1034 (2010), Modifications of gyre circulation by sub-mesoscale physics, *Ocean Modelling*,
1035 *34*(1-2), 1–15.
- 1036 Lévy, M., R. Ferrari, P. J. Franks, A. P. Martin, and P. Rivière (2012), Bringing physics to
1037 life at the submesoscale, *Geophysical Research Letters*, *39*(14).
- 1038 Lumpkin, R., and S. Elipot (2010), Surface drifter pair spreading in the north atlantic,
1039 *Journal of Geophysical Research: Oceans*, *115*(C12).

- 1040 Lumpkin, R., T. Özgökmen, and L. Centurioni (2017), Advances in the application of sur-
 1041 face drifters, *Annual review of marine science*, *9*, 59–81.
- 1042 Ma, J., H. Xu, C. Dong, P. Lin, and Y. Liu (2015), Atmospheric responses to oceanic ed-
 1043 dies in the kuroshio extension region, *Journal of Geophysical Research: Atmospheres*,
 1044 *120*(13), 6313–6330.
- 1045 Mahadevan, A. (2016), The impact of submesoscale physics on primary productivity of
 1046 plankton, *Annual review of marine science*, *8*, 161–184.
- 1047 Martin, A. C. H., C. Gommenginger, J. Marquez, S. Doody, V. Navarro, and C. Buck
 1048 (2016), Wind-wave-induced velocity in atisar ocean surface currents: First experimental
 1049 evidence from airborne campaign, *Journal of Geophysical Research: Oceans*, *21*, 1640–
 1050 1653.
- 1051 Maximenko, N. A., B. Bang, and H. Sasaki (2005), Observational evidence of alternating
 1052 zonal jets in the world ocean, *Geophysical research letters*, *32*(12).
- 1053 Maximenko, N. A., M. Oleg V., N. Pearn P., and S. Hideharu (2008), Stationary
 1054 mesoscale jet-like features in the ocean, *Geophysical research letters*, *35*.
- 1055 McGillicuddy Jr, D. J. (2016), Mechanisms of physical-biological-biogeochemical interac-
 1056 tion at the oceanic mesoscale, *Annual review of marine science*.
- 1057 McWilliams, J., F. Colas, and M. Molemaker (2009), Cold filamentary intensification and
 1058 oceanic surface convergence lines, *Geophysical Research Letters*, *36*(18).
- 1059 McWilliams, J. C. (1989), Statistical properties of decaying geostrophic turbulence, *Jour-
 1060 nal of Fluid Mechanics*, *198*, 199–230.
- 1061 McWilliams, J. C. (2016), Submesoscale currents in the ocean, *Proc. R. Soc. A*, *472*(2189),
 1062 20160,117.
- 1063 Menesguen, C., A. Delpech, F. Marin, S. Cravatte, R. Schopp, and Y. Morel (2018), Ob-
 1064 servations and mechanisms for the formation of deep equatorial and tropical circulation,
 1065 *Earth and Space Science*.
- 1066 Mensa, J. A., Z. Garraffo, A. Griffa, T. M. Özgökmen, A. Haza, and M. Veneziani (2013),
 1067 Seasonality of the submesoscale dynamics in the gulf stream region, *Ocean Dynamics*,
 1068 *63*(8), 923–941.
- 1069 Merlis, T., and T. Schneider (2009), Scales of linear baroclinic instability and macroturbu-
 1070 lence in dry atmospheres, *Journal of the Atmospheric Sciences*, *66*, 1821–1833.
- 1071 Mezić, I., S. Loire, V. Fonoberov, and P. Hogan (2010), A new mixing diagnostic and gulf
 1072 oil spill movement, *Science*, *330*, 486–489.
- 1073 Minobe, S., A. Kuwano-Yoshida, N. Komori, S.-P. Xie, and R. J. Small (2008), Influence
 1074 of the gulf stream on the troposphere, *Nature*, *452*(7184), 206.
- 1075 Molemaker, M. J., J. C. McWilliams, and X. Capet (2010), Balanced and unbalanced
 1076 routes to dissipation in an equilibrated eady flow, *Journal of Fluid Mechanics*, *654*, 35–
 1077 63.
- 1078 Morrow, R., and P.-Y. Le Traon (2012), Recent advances in observing mesoscale ocean
 1079 dynamics with satellite altimetry, *Advances in Space Research*, *50*(8), 1062–1076.
- 1080 Müller, M., B. K. Arbic, J. G. Richman, J. F. Shriver, E. L. Kunze, R. B. Scott, A. J.
 1081 Wallcraft, and L. Zamudio (2015), Toward an internal gravity wave spectrum in global
 1082 ocean models, *Geophysical Research Letters*, pp. 3474–3481.
- 1083 Nakamura, H., T. Sampe, A. Goto, W. Ohfuchi, and S.-P. Xie (2008), On the importance
 1084 of midlatitude oceanic frontal zones for the mean state and dominant variability in the
 1085 tropospheric circulation, *Geophysical Research Letters*, *35*(15).
- 1086 Özgökmen, T. M., A. C. Poje, P. F. Fischer, H. Childs, H. Krishnan, C. Garth, A. C. Haza,
 1087 and E. Ryan (2012), On multi-scale dispersion under the influence of surface mixed
 1088 layer instabilities and deep flows, *Ocean Modelling*, *56*, 16–30.
- 1089 Panetta, R. L. (1993), Zonal jets in wide baroclinically unstable regions: Persistence and
 1090 scale selection, *Journal of the atmospheric sciences*, *50*(14), 2073–2106.
- 1091 Pierrehumbert, R. T., I. M. Held, and K. L. Swanson (1994), Spectra of local and nonlocal
 1092 two-dimensional turbulence, *Chaos, Solitons & Fractals*, *4*, 1111–Cambridge U–1116.

- 1093 Poje, A., M. Ā. Tamay, L. Bruce, H. Brian, R. Edward H., H. Angelique C., J. Gregg A.,
 1094 R. A. J. H. M., O. Maria Josefina, N. Guillaume, G. Annalisa, B.-V. Francisco J.,
 1095 C. Shuyi S., C. Emanuel, H. Patrick J., K. Albert D., . H. Helga S, and M. Arthur J.
 1096 (2014), Submesoscale dispersion in the vicinity of the deepwater horizon spill, *Proceed-*
 1097 *ing of the National Academy of Sciences*, *111*(35), 12,693–12,698.
- 1098 Polzin, K. L., and Y. Lvov (2011), Toward regional characterizations of the oceanic inter-
 1099 nal wavefield, *Review of Geophysics*, *49*, <https://doi.org/10.1029/2010RG000329>.
- 1100 Ponte, A. L., and P. Klein (2015), Incoherent signature of internal tides on sea level in
 1101 idealized numerical simulations, *Geophysical Research Letters*, *42*(5), 1520–1526.
- 1102 Qiu, B., and S. Chen (2005), Eddy-induced heat transport in the subtropical north pa-
 1103 cific from argo, tmi and altimetry measurements, *Journal of Physical Oceanography*,
 1104 *35*, 458–473.
- 1105 Qiu, B., S. Chen, P. Klein, H. Sasaki, and Y. Sasai (2014), Seasonal mesoscale and sub-
 1106 mesoscale eddy variability along the north pacific subtropical countercurrent, *Journal of*
 1107 *Physical Oceanography*, *44*(12), 3079–3098.
- 1108 Qiu, B., S. Chen, P. Klein, C. Ubelmann, L.-L. Fu, and H. Sasaki (2016), Reconstructabil-
 1109 ity of three-dimensional upper-ocean circulation from swot sea surface height measure-
 1110 ments, *Journal of Physical Oceanography*, *46*, 947–963.
- 1111 Qiu, B., T. Nakano, S. Chen, and P. Klein (2017), Submesoscale transition from
 1112 geostrophic flows to internal waves in the northwestern pacific upper ocean, *Nature*
 1113 *communications*, *8*, 14,055.
- 1114 Qiu, B., S. Chen, P. Klein, J. Wang, H. Torres, L.-L. Fu, and D. Menemenlis (2018), Sea-
 1115 sonality in transition scale from balanced to unbalanced motions in the world ocean,
 1116 *Journal of Physical Oceanography*, *48*(3), 591–605.
- 1117 Ray, R. D., and G. T. Mitchum (1997), Surface manifestation of internal tides in the deep
 1118 ocean: Observations from altimetry and island gauges, *Progress in Oceanography*, *40*(1-
 1119 4), 135–162.
- 1120 Ray, R. D., and E. D. Zaron (2016), M2 internal tides and their observed wavenumber
 1121 spectra from satellite altimetry, *Journal of Physical Oceanography*, *46*(1), 3–22.
- 1122 Renault, L., J. McWilliams, and J. Gula (2018), Dampening of submesoscale currents by
 1123 air-sea stress coupling in the californian upwelling system, *Scientific Reports*, *8*, 13,388.
- 1124 Rhines, P. B. (1975), Waves and turbulence on a beta-plane, *Journal of Fluid Mechanics*,
 1125 *69*(3), 417–443.
- 1126 Rhines, P. B. (1979), Geostrophic turbulence., *Annual Review of Fluid Mechanics*, *11*, 401–
 1127 441.
- 1128 Richman, J. G., B. K. Arbic, J. F. Shriver, E. J. Metzger, and A. J. Wallcraft (2012), In-
 1129 ferring dynamics from the wavenumber spectra of an eddying global ocean model with
 1130 embedded tides, *Journal of Geophysical Research: Oceans*, *117*(C12).
- 1131 Rocha, C. B., S. T. Gille, T. K. Chereskin, and D. Menemenlis (2016a), Seasonality of
 1132 submesoscale dynamics in the kuroshio extension, *Geophysical Research Letters*, *43*(21),
 1133 11–304.
- 1134 Rocha, C. B., T. K. Chereskin, S. T. Gille, and D. Menemenlis (2016b), Mesoscale to sub-
 1135 mesoscale wavenumber spectra in drake passage, *Journal of Physical Oceanography*,
 1136 *46*(2), 601–620.
- 1137 Rocha, C. B., G. L. Wagner, and W. R. Young (2018), Stimulated generation: extraction
 1138 of energy from balanced flow by near-inertial waves, *Journal of Fluid Mechanics*, *847*,
 1139 417–451.
- 1140 Rodríguez, E., A. Wineteer, D. Perkovic-Martin, T. Gál, B. W. Stiles, N. Niamsuwan,
 1141 and R. R. Monje (2018), Estimating ocean vector winds and currents using a ka-band
 1142 pencil-beam doppler scatterometer, *Remote Sensing*, *10*(4), 576.
- 1143 Roulet, G., J. C. McWilliams, X. Capet, and M. J. Molemaker (2012), Properties of
 1144 steady geostrophic turbulence with isopycnal outcropping, *Journal of Physical Oceanog-*
 1145 *raphy*, *42*(1), 18–38.

- 1146 Salmon, R. (1980), Baroclinic instability and geostrophic turbulence, *Geophysical & Astro-*
 1147 *physical Fluid Dynamics*, 15(1), 167–211.
- 1148 Sasaki, H., P. Klein, B. Qiu, and Y. Sasai (2014), Impact of oceanic-scale interactions on
 1149 the seasonal modulation of ocean dynamics by the atmosphere, *Nature communications*,
 1150 5, ncomms6636.
- 1151 Savage, A. C., B. K. Arbic, M. H. Alford, J. K. Ansong, J. T. Farrar, D. Menemenlis,
 1152 A. K. O’Rourke, J. G. Richman, J. F. Shriver, G. Voet, et al. (2017a), Spectral decom-
 1153 position of internal gravity wave sea surface height in global models, *Journal of Geo-*
 1154 *physical Research: Oceans*, 122(10), 7803–7821.
- 1155 Savage, A. C., B. K. Arbic, J. G. Richman, J. F. Shriver, M. H. Alford, M. C. Buijsman,
 1156 J. Thomas Farrar, H. Sharma, G. Voet, A. J. Wallcraft, et al. (2017b), Frequency con-
 1157 tent of sea surface height variability from internal gravity waves to mesoscale eddies,
 1158 *Journal of Geophysical Research: Oceans*, 122(3), 2519–2538.
- 1159 Schneider, T., and C. C. Walker (2006), Self-organization of atmospheric macroturbulence
 1160 into critical states of weak nonlinear eddy–eddy interactions, *Journal of the Atmo-*
 1161 *spheric Sciences*, 63, 1569–1586.
- 1162 Scott, R. (2006), Local and nonlocal advection of a passive scalar, *Physics of Fluids*,
 1163 18(11), 116,601.
- 1164 Scott, R. B., and F. Wang (2005), Direct evidence of an oceanic inverse kinetic energy
 1165 cascade from satellite altimetry, *Journal of Physical Oceanography*, 35(9), 1650–1666.
- 1166 Smith, K. S. (2007), The geography of linear baroclinic instability in earth’s oceans, *Jour-*
 1167 *nal of Marine Research*, 65(5), 655–683.
- 1168 Smith, K. S., and G. K. Vallis (2001), The scales and equilibration of midocean eddies:
 1169 Freely evolving flow, *Journal of Physical Oceanography*, 31(2), 554–571.
- 1170 Stammer, D., R. Tokmakian, A. Semtner, and C. Wunsch (1996), How well does a 1/4°
 1171 global circulation model simulate large-scale oceanic observations?, *Journal of Geophys-*
 1172 *ical Research: Oceans*, 101(C11), 25,779–25,811.
- 1173 Stammer, D., R. Ray, O. B. Andersen, B. Arbic, W. Bosch, L. Carrère, Y. Cheng,
 1174 D. Chinn, B. Dushaw, G. Egbert, et al. (2014), Accuracy assessment of global
 1175 barotropic ocean tide models, *Reviews of Geophysics*, 52(3), 243–282.
- 1176 Stone, P. H. (1966), Frontogenesis by horizontal wind deformation fields, *Journal of the*
 1177 *Atmospheric Sciences*, 23(5), 455–465.
- 1178 Su, Z., J. Wang, P. Klein, A. F. Thompson, and D. Menemenlis (2018), Ocean subme-
 1179 soscales as a key component of the global heat budget, *Nature communications*, 9(1),
 1180 775.
- 1181 Taylor, S., and D. Straub (2016), Forced near-inertial motion and dissipation of low-
 1182 frequency kinetic energy in a wind-driven channel flow, *Journal of Physical Oceanog-*
 1183 *raphy*, 46(1), 79–93.
- 1184 Tennekes, H., and J. L. Lumley (1974), *A first course in turbulence*, MIT Press.
- 1185 Thomas, L. N. (2017), On the modifications of near-inertial waves at fronts: implications
 1186 for energy transfer across scales, *Ocean Dynamics*, 67(10), 1335–1350.
- 1187 Thompson, A. F., A. Lazar, C. Buckingham, A. C. Naveira Garabato, G. M. Damerell,
 1188 and K. J. Heywood (2016), Open-ocean submesoscale motions: A full seasonal cycle of
 1189 mixed layer instabilities from gliders, *Journal of Physical Oceanography*, 46(4), 1285–
 1190 1307.
- 1191 Torres, H., P. Klein, D. Menemenlis, B. Qiu, Z. Su, J. Wang, S. Chen, and L.-L. Fu
 1192 (2018), Partitioning ocean motions into balanced motions and internal gravity waves
 1193 from space, *Journal of Geophysical Research*.
- 1194 Tulloch, R., and K. Smith (2006), A theory for the atmospheric energy spectrum: Depth-
 1195 limited temperature anomalies at the tropopause, *Proceedings of the National Academy*
 1196 *of Sciences*, 103(40), 14,690–14,694.
- 1197 Tulloch, R., J. Marshall, C. Hill, and K. S. Smith (2011), Scales, growth rates, and spec-
 1198 tral fluxes of baroclinic instability in the ocean, *Journal of Physical Oceanography*,
 1199 41(6), 1057–1076.

- 1200 Ubelmann, C., P. Klein, and L.-L. Fu (2015), Dynamic interpolation of sea surface height
1201 and potential applications for future high-resolution altimetry mapping, *Journal of Atmo-*
1202 *spheric and Oceanic Technology*, *32*, 177–184.
- 1203 Vallis, G. K. (2017), *Atmospheric and oceanic fluid dynamics*, Cambridge University Press.
- 1204 Wagner, G., and W. Young (2016), A three-component model for the coupled evolution
1205 of near-inertial waves, quasi-geostrophic flow and the near-inertial second harmonic,
1206 *Journal of Fluid Mechanics*, *802*, 806–837.
- 1207 Wang, J., L.-L. Fu, H. Torres, S. Chen, B. Qiu, and D. Menemenlis (2019), On the spatial
1208 scale to be resolved by the surface water and ocean topography ka-band fadar interfer-
1209 ometer, *Journal of Atmospheric and Oceanic Technology*, *36*, 87–99.
- 1210 Whitt, D. B., and L. N. Thomas (2015), Resonant generation and energetics of wind-
1211 forced near-inertial motions in a geostrophic flow, *Journal of Physical Oceanography*,
1212 *45*(1), 181–208.
- 1213 Wortham, C., and C. Wunsch (2014), A multidimensional spectral description of ocean
1214 variability, *Journal of Physical Oceanography*, *44*(3), 944–966.
- 1215 Wunsch, C. (2002), Ocean observations and the climate forecast problem, *INTERNA-*
1216 *TIONAL GEOPHYSICS SERIES*, *83*, 233–248.
- 1217 Wunsch, C. (2009), The oceanic variability spectrum and transport trends, *Atmosphere-*
1218 *ocean*, *47*(4), 281–291.
- 1219 Wunsch, C. (2010), Toward a midlatitude ocean frequency–wavenumber spectral density
1220 and trend determination, *Journal of Physical Oceanography*, *40*(10), 2264–2281.
- 1221 Xie, J.-H., and J. Vanneste (2015), A generalised-lagrangian-mean model of the interac-
1222 tions between near-inertial waves and mean flow, *Journal of Fluid Mechanics*, *774*, 143–
1223 169.
- 1224 Xu, Y., and L.-L. Fu (2012), The effects of altimeter instrument noise on the estimation
1225 of the wavenumber spectrum of sea surface height, *Journal of Physical Oceanography*,
1226 *42*(12), 2229–2233.
- 1227 Young, W., and M. B. Jelloul (1997), Propagation of near-inertial oscillations through a
1228 geostrophic flow, *Journal of marine research*, *55*(4), 735–766.
- 1229 Zaron, E. D., and G. D. Egbert (2014), Time-variable refraction of the internal tide at the
1230 hawaiian ridge, *Journal of Physical Oceanography*, *44*(2), 538–557.
- 1231 Zhai, X., R. J. Greatbatch, and J.-D. Kohlmann (2008), On the seasonal variability of
1232 eddy kinetic energy in the gulf stream region, *Geophysical Research Letters*, *35*(24).